Bachelor Thesis

Ab-initio Calculation of Weyl Points in T_d-MoTe$_2$ Semimetal and Transition to $1T'$-Phase Induced by Coherent Phonons

Sam Benedikt Fiedler

Christian-Albrechts-Universität zu Kiel

Fakultät für Mathematik und Naturwissenschaften

Institut für Physik

First Examiner: Prof. Dr. Fabio Caruso

Second Examiner: Prof. Dr. Stefan Heinze

Date of Submission: 18.07.2025

Meiner Großmutter Irmtraud Voshage

Abstract

In this work, we investigate the electronic structure and lattice dynamics of $MoTe_2$ in the noncentrosymmetric T_d-phase using *ab-initio* methods. First, we compute the band structures of the T_d- und $1T'$-phase within Density Functional Theory using carefully converged parameters. By including Spin-Orbit-Coupling and performing a subsequent Wannier interpolation, we precisely locate two Weyl-point pairs per Brillouin-zone quadrant at energies just above the Fermi level.

The lattice vibrations are calculated via Density Functional Perturbation Theory, delivering 36 phonon modes. In particular, low-frequency B_1 shear modes combine to induce a lattice distortion that drives the phase-transition from T_d to the centrosymmetric $1T'$-phase (space group $P2_1$). These results constitute the theoretical demonstration of an ultrafast, phonon-induced topological switch in $MoTe_2$.

Zusammenfassung

In dieser Arbeit wird mit *ab-initio*-Methoden die elektronische Struktur und die Phononendynamik von MoTe_2 in der nichtzentrumssymmetrischen T_d-Phase untersucht. Zunächst werden mithilfe der Density Functional Theory und sorgfältig konvergierter Parameter die Bandstrukturen der T_d- und $1T'$-Phase berechnet. Durch Einbeziehung des Spin-Orbit-Coupling und anschließende Wannier-Interpolation lassen sich im Impulsraum zwei Weyl-Paare je Quadrant im Impulsraum, sowie Energien knapp oberhalb des Fermi-Niveaus präzise lokalisieren.

Die Gitterschwingungen werden mit der Density Functional Perturbation Theory berechnet und liefern 36 Phononenmoden. Besonders niederfrequente B_1-Schermoden induzieren in Kombination eine Gitterverzerrung, die den Phasenübergang von T_d nach $1T'$ in die zentrumsymmetrische Raumgruppe $P2_1$ ermöglicht. Die vorgestellten Ergebnisse demonstrieren theoretisch die Realisierbarkeit eines ultraschnellen, phononeninduzierten Topologieschalters in MoTe_2.

Contents

List of abbreviations

$MoTe_2$	Molybdenum Ditelluride
DFT	Density Functional Theory
DFPT	Density Functional Perturbation Theory
HAU	Hartree Atomic Units
SOC	Spin-Orbit-Coupling
VdW	Van-der-Waals
W90	Wannier90
QE	Quantum ESPRESSO
WP	Weyl-Point
WSM	Weyl Semimetal
TMD	Transition-Metal Dichalcogenide
MLWF	maximally localized Wannier functions
SCF	Self-Consistent Field
NSCF	Non-Self-Consistent Field
BOA	Born-Oppenheimer-Approximation
PT	phase-transition
PAW	Projector Augmented-Wave
GGA	Generalized Gradient-Approximation
PBE	Perdew-Burke-Ernzerhof

1 Introduction

1.1 Historic development of Weyl-points

After Paul Dirac introduced his famous Dirac equation in 1928, Hermann Weyl proposed the Weyl equation one year later [52]. Unlike the Dirac equation, which describes massive fermions (particles with half-integer spin), the Weyl equation covers massless fermions. In 1937, Conyers Herring predicted Weyl fermions as quasiparticles in condensed matter [20].

Mistakenly, the Weyl equation was long thought to describe neutrinos, until a small neutrino mass was detected in 1998. A major breakthrough came in 2015, when TaAs was predicted to be a Weyl semimetal [25] and experimentally confirmed [24]. This milestone inspired many research groups to intensify their studies, leading to predictions and confirmations of further candidates such as WTe_2 [43] and Molybdenum Ditelluride ($MoTe_2$) [23, 39, 44, 12] as Weyl Semimetal (WSM).

WSMs are of great interest and continue to be examined for additional properties [13]. Currently, they play a significant role in spintronics [29], but even more so in fundamental research, since they constitute a new class of materials distinct from classical semiconductors. They are known for their unique transport phenomena derived from the Weyl equation, including the anomalous Hall effect [32, 8, 11], the chiral anomaly [3, 34, 26], and negative magnetoresistance [30]. Therefore, finding new materials that act as WSM is of great interest.

Another exciting research field associated with WSMs is quantum computing [40]. Due to their topological properties and the ability to host robust states, WSMs may contribute to quantum computer development. In particular, chiral excitations and topologically protected states could be utilized to create error-resilient quantumbits. These attributes make WSM - especially $MoTe_2$ - promising candidates for future applications in quantum information processing [46].

1.2 Motivation

In this work, we investigate the Transition-Metal Dichalcogenide (TMD) $MoTe_2$, which can be exfoliated into a two-dimensional material. TMDs are compounds of a transition metal and a chalcogen, always taking the form MX_2 (M = transition metal, X = chalcogen). Van-der-Waals (VdW) forces stabilize stacked monolayers, and these layers can be shifted by external stimuli, thereby tuning the material's electronic properties. TMDs exhibit a rich variety of phenomena, including superconductivity, magnetism, and nontrivial topological order.

Most TMDs can be synthesized or modulated in multiple symmetry phases. $MoTe_2$ exists in three phases [7]. Under ambient pressure and room-temperature crystallization, the $2H$ phase forms and is thermodynamically the most stable. The $1T'$ phase is metastable, stable only above about $900\,\mathrm{K}$, and is centrosymmetric with space group $P2_1$ (or C_{2h}^2). Cooling the $1T'$ phase below $-20\,^\circ\mathrm{C}$ yields the noncentrosymmetric T_d phase [53].

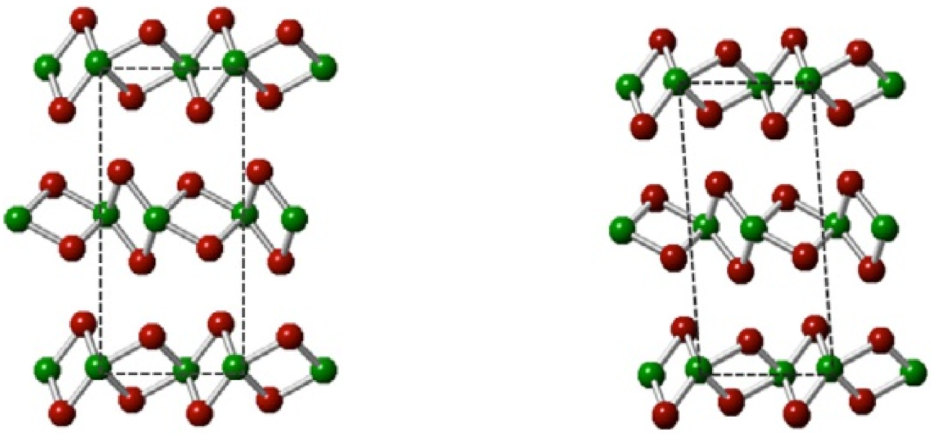

(a) Crystal structure of $MoTe_2$ in the T_d phase. Mo atoms in green, Te atoms in red.

(b) Crystal structure of $MoTe_2$ in the $1T'$ phase. Mo atoms in green, Te atoms in red.

Figure 1.1: Comparison of $MoTe_2$ crystal structures in the $1T'$ and T_d phases [12].

As shown in Figure 1.1, the $1T'$ phase is a distorted variant of the T_d structure. The T_d phase belongs to space group $Pmn2_1$ (or C_{2v}^7), which breaks inversion symmetry, a prerequisite for the emergence of Weyl-Point (WP) via Spin-Orbit-Coupling (SOC) [35]. Breaking either inversion or time-reversal symmetry suffices. Spin-Orbit-Coupling lifts band degeneracies, bringing adjacent bands into contact and producing Weyl points WP.

WPs are pointlike crossings of valence and conduction bands in momentum space. They always appear in pairs of opposite chirality, and on a material's surface they connect by Fermi arcs, yielding open Fermi contours.

In WTe_2, ultrafast phonon-driven topological phase-transition (PT) have been simulated and demonstrated [41], rapidly altering the material's topology. Such manipulation could serve as a topological switch for dissipationless electronics and robust quantum computers. To realize these transitions, terahertz laser pulses are used to excite coherent, low-frequency shear modes, which can drive Weyl points in the metastable T_d phase together and annihilate them, thereby stabilizing the centrosymmetric $1T'$ phase.

1.3 Goal of this work

In this work, we use ab-initio calculations to establish the existence and locate the WPs in the T_d phase of $MoTe_2$ in momentum space. Furthermore, we examine the phase-transition (PT) from the T_d phase to the $1T'$ phase driven by coherent, low-frequency shear phonon modes. For this purpose, we employ Density Functional Theory (DFT), Density Functional Perturbation Theory (DFPT), and Wannier-based band-structure interpolation.

2 Theoretical foundations

In this section, we present the theoretical framework used to calculate the electronic properties of $\mathrm{MoTe_2}$.

2.1 Density Functional Theory

To simplify the equations in this section, we employ the Hartree Atomic Units (HAU). These are defined as:

$$\hbar = m_e = e^2 = \frac{1}{4\pi\epsilon_0} = 1, \tag{2.1}$$

where $\hbar$ is the reduced Planck constant, m_e the electron mass, e the elementary charge, and ϵ_0 the vacuum permittivity.

First, we review the fundamentals of DFT, based on a lecture by *Prof. Dr. Eckhard Pehlke* [36] and the book *Materials Modeling using Density Functional Theory* [17] by *Feliciano Giustino*. Next, we discuss interpolation methods. Then, we briefly explain DFPT [9], which allows us to simulate lattice dynamics. Finally, we cover special topics that are specifically required for this work.

2.1.1 Many body Schrödinger equation

Calculating the properties of molecular systems at the microscopic level with high precision poses a tremendous challenge. Thanks to approximations and efficient algorithms, DFT can yield highly accurate results in a reasonable time frame. The foundation of these methods is the time-dependent many-body Schrödinger equation:

$$\begin{aligned} i\hbar\partial_t\Psi(\{\mathbf{R(t)}\},\{\mathbf{x(t)}\},t) &= \hat{H}_{\text{tot}}\Psi(\{\mathbf{R(t)}\},\{\mathbf{x(t)}\},t) \\ &= E_{\text{tot}}\Psi(\{\mathbf{R(t)}\},\{\mathbf{x(t)}\},t) \end{aligned} \tag{2.2}$$

where $\{\mathbf{R(t)}\} = \{\mathbf{R_1}, \mathbf{R_2}, \dots, \mathbf{R_{N_{\text{Ion}}}}\}$ are the coordinates of N_{Ion} ions and $\{\mathbf{x(t)}\} = (\{\mathbf{r(t)}\}, \sigma)$ represents the electronic coordinates $\{\mathbf{r(t)}\} = \{\mathbf{r_1}, \mathbf{r_2}, \dots, \mathbf{r_{N_{\text{El}}}}\}$ for N_{El}

electrons including spin $\sigma \in \{\uparrow, \downarrow\}$.
In this work, only time-independent DFT is used. Henceforth, let $\psi := \Psi(t = 0)$. We then have:

$$\hat{H}_{\text{tot}}\psi_0(\{\mathbf{R}(\mathbf{0})\}, \{\mathbf{x}(\mathbf{0})\}) = E(t = 0)\psi_0(\{\mathbf{R}(\mathbf{0})\}, \{\mathbf{x}(\mathbf{0})\}) \tag{2.3}$$

The total Hamiltonian must capture all ionic and electronic energies as well as their mutual interactions. Accordingly, it can be described as:

$$\begin{aligned}\hat{H}_{\text{tot}} &= \hat{T}_{\text{tot}} + \hat{V}_{\text{tot}} \\ &= \hat{T}_{\text{Ion}} + \hat{T}_{\text{El}} + \hat{V}_{\text{Ion}-\text{Ion}} + \hat{V}_{\text{El}-\text{El}} + \hat{V}_{\text{Ion}-\text{El}} \end{aligned} \tag{2.4}$$

The kinetic operators $\hat{T}_{\text{tot}}$ and the interaction operator $\hat{V}_{\text{tot}}$ together exactly describe the isolated, non-relativistic, spin-unpolarized system. The individual terms are defined as:

$$\hat{T}_{\text{Ion}} = -\sum_{I=1}^{N_{\text{Ion}}} \frac{1}{2M_I} \nabla^2_{\mathbf{R}_I}, \tag{2.5}$$

$$\hat{T}_{\text{El}} = -\sum_{i=1}^{N_{\text{El}}} \frac{1}{2} \nabla^2_{\mathbf{r}_i}, \tag{2.6}$$

$$\hat{V}_{\text{Ion}-\text{Ion}} = \frac{1}{2} \sum_{I,J=1}^{N_{\text{Ion}}} \frac{Z_I Z_J}{|\mathbf{R}_I - \mathbf{R}_J|} \tag{2.7}$$

$$\hat{V}_{\text{El}-\text{El}} = \frac{1}{2} \sum_{i,j=1}^{N_{\text{El}}} \frac{1}{|\mathbf{r}_i - \mathbf{r}_j|} \tag{2.8}$$

$$\hat{V}_{\text{Ion}-\text{El}} = -\sum_{i=1}^{N_{\text{El}}} \sum_{I=1}^{N_{\text{Ion}}} \frac{Z_I}{|\mathbf{r}_i - \mathbf{R}_I|}. \tag{2.9}$$

The ionic charges Z_I and masses M_I must be included explicitly; electron charges and masses are implicit in the HAU. The factor $\frac{1}{2}$ in eqs. (2.7) and (2.8) results from double counting.

2.1.2 Born-Oppenheimer-Approximation

Electronic motions are roughly 1800 times faster than nuclear motions. Therefore, for molecular systems it suffices to treat the nuclei as “frozen” in a first approximation. The Born-Oppenheimer-Approximation (BOA) [6] implements this by using a

Hamiltonian with fixed nuclear coordinates:

$$\hat{H}_{\text{BOA}} := \hat{H}(\{\mathbf{R}\}) = \hat{T}_{\text{El}} + \hat{V}_{\text{Ion}-\text{El}}(\{\mathbf{R}\}) + \hat{V}_{\text{El}-\text{El}} \tag{2.10}$$

$$=: \hat{T} + \hat{V} + \hat{W}. \tag{2.11}$$

Accordingly, the wavefunction depends only on the electronic coordinates, and we obtain the eigenvalue problem:

$$\hat{H}_{\text{BOA}}\, \psi_{\{\mathbf{R}\},\mu}(\{\mathbf{r}\}) = E_\mu(\{\mathbf{R}\})\, \psi_{\{\mathbf{R}\},\mu}(\{\mathbf{r}\}), \tag{2.12}$$

for states $\mu \in \{0, 1, 2, \ldots, N_{\text{El}}\}$, assuming the ground-state energy ($\mu = 0$) is non-degenerate. In subsequent expressions for the same system, the explicit dependence on $\{\mathbf{R}\}$ is dropped for brevity.

2.1.3 Hohenberg-Kohn Theorems

The BOA already simplifies the computation enormously. However, one still must solve the Schrödinger equation for all electrons, and the computational effort grows exponentially with the number of electrons. In the 1960s, Hohenberg and Kohn developed a method that reduces this scaling to linear. There are two theorems [22] whose statements form the foundation of DFT:

Hohenberg-Kohn Theorem I: The ground-state energy E_0 is (after fixing the additive constant in the one-body potential) a functional of the ground-state electron density $n_0(\mathbf{r})$.

Proof: Suppose the wavefunction is simultaneously the ground state for the potentials $V^{(1)}$ and $V^{(2)} \neq V^{(1)} + \text{const}$. Then it follows:

$$\begin{aligned} \hat{H}^{(1)}\psi_0 &:= (\hat{T} + \hat{V}^{(1)} + \hat{W})\psi_0 = E_0^{(1)}\psi_0 \\ \hat{H}^{(2)}\psi_0 &:= (\hat{T} + \hat{V}^{(2)} + \hat{W})\psi_0 = E_0^{(2)}\psi_0 \\ \Rightarrow (\hat{V}^{(2)} - \hat{V}^{(1)})\psi_0 &= (E_0^{(2)} - E_0^{(1)})\psi_0 \end{aligned} \tag{2.13}$$

Now assume that two different wavefunctions $\psi_0^{(1)}$ and $\psi_0^{(2)}$ yield the same ground-state energy. Then we have:

$$E_0^{(1)} = \left\langle \psi_0^{(1)} \right| \hat{H}^{(1)} \left| \psi_0^{(1)} \right\rangle, \quad E_0^{(2)} = \left\langle \psi_0^{(2)} \right| \hat{H}^{(2)} \left| \psi_0^{(2)} \right\rangle \tag{2.14}$$

The Ritz variational principle states $E_0 = \min \langle \psi_\mu | \hat{H} | \psi_\mu \rangle$ subject to $\langle \psi_\mu | \psi_\mu \rangle = 1$. Therefore, all energies not in the ground state must be larger. Accordingly, it follows that:

$$\begin{aligned} E_0^{(1)} &= \left\langle \psi_0^{(1)} \middle| \hat{T} + \hat{V}^{(2)} + \hat{W} \middle| \psi_0^{(1)} \right\rangle + \left\langle \psi_0^{(1)} \middle| \hat{V}^{(1)} - \hat{V}^{(2)} \middle| \psi_0^{(1)} \right\rangle \\ &= \left\langle \psi_0^{(1)} \middle| \hat{T} + \hat{V}^{(2)} + \hat{W} \middle| \psi_0^{(1)} \right\rangle + \int (V^{(1)}(\mathbf{r}) - V^{(2)}(\mathbf{r})) n(\mathbf{r}) \,\mathrm{d}\mathbf{r} \\ &> \left\langle \psi_0^{(2)} \middle| \hat{T} + \hat{V}^{(2)} + \hat{W} \middle| \psi_0^{(2)} \right\rangle + \int (V^{(1)}(\mathbf{r}) - V^{(2)}(\mathbf{r})) n(\mathbf{r}) \,\mathrm{d}\mathbf{r} \\ &= E_0^{(2)} + \int (V^{(1)}(\mathbf{r}) - V^{(2)}(\mathbf{r})) n(\mathbf{r}) \,\mathrm{d}\mathbf{r} \end{aligned} \tag{2.15}$$

Also it follows:

$$E_0^{(2)} > E_0^{(1)} + \int (V^{(2)} - V^{(1)}) n(\mathbf{r}) \,\mathrm{d}\mathbf{r} \tag{2.16}$$

And together it follows: $E_0^{(1)} > E_0^{(1)}$, a contradiction. Thus Theorem I is proven.

Hohenberg-Kohn Theorem II: Let $n_0(\mathbf{r})$ be the ground-state density corresponding to the one-particle potential V. Then, for any particle density $n(\mathbf{r})$ in the domain of the relevant functionals, it holds:

$$E_{V_0}[n] \geq E_{V_0}[n_0] =: E_0[n_0] \tag{2.17}$$

Proof: The particle density is, according to Theorem I, associated via the potential W_0 with the ground-state density n_0 and a ground-state wavefunction ψ_0.

$$\begin{aligned} E_{V_0}[n] &= \langle \psi_\mu | \hat{T} + \hat{V}_0 + \hat{W} | \psi_\mu \rangle , \quad \mu \neq 0 \\ &\geq \langle \psi_0 | \hat{T} + \hat{V}_0 + \hat{W} | \psi_0 \rangle = E_{V_0}[n_0] = E_0[n_0] \end{aligned} \tag{2.18}$$

Thus, the energy can be minimized with respect to the particle density.

2.1.4 Kohn-Sham equations

Kohn and Sham developed a method [28] to minimize the energy with respect to the particle density. The energy functional can also be written as:

$$E_V[n] = T_S[n] + E_H[n] + E_{XC}[n] + \int V(\mathbf{r}) n(\mathbf{r}) \,\mathrm{d}\mathbf{r} \,, \tag{2.19}$$

where $T_S[n]$ describes the non-interacting system, $E_H[n]$, called the Hartree energy, represents the classical Coulomb interaction, and $E_{XC}[n]$ is the exchange-correlation energy that collects all remaining effects. Together, the energy functional reads:

$$E_V[n] = \sum_{i=1}^{\mathrm{N_{El}}} \langle\psi_\mu| \frac{\nabla^2}{2} |\psi_\mu\rangle + \frac{1}{2}\int\int \frac{n(\mathbf{r})n(\mathbf{x}')}{|\mathbf{r}-\mathbf{x}'|}\,\mathrm{d}\mathbf{r} + E_{XC}[n] + \int V(\mathbf{r})n(\mathbf{r})\,\mathrm{d}\mathbf{r}\,, \tag{2.20}$$

for orthonormal single-particle eigenstates $\{\psi_1, \ldots, \psi_{N_{\mathrm{El}}}\}$ with $\langle\psi_\mu|\psi_\nu\rangle = \delta_{\mu\nu}$. These then form the total wavefunction as a Slater determinant:

$$\psi^{SL} = \frac{1}{\sqrt{N_{\mathrm{El}}!}} \det(\psi_1(\mathbf{x_1})\psi_2(\mathbf{x_2})\cdots\psi_{\mathrm{N_{El}}}(\mathbf{x}_{\mathrm{N_{El}}})). \tag{2.21}$$

After Hohenberg-Kohn I, the energy in the ground state is minimized. By the variational principle we have: $\delta E_V[n] = 0$. This yields an effective potential

$$V_{\mathrm{eff}}(\mathbf{r}) = V(\mathbf{r}) + V_H(\mathbf{r}) + V_{XC}(\mathbf{r}) \tag{2.22}$$

with $V_H(\mathbf{r}) = \frac{\delta E_H[n]}{\delta n(\mathbf{r})}$, $V_{XC}(\mathbf{r}) = \frac{\delta E_{XC}[n]}{\delta n(\mathbf{r})}$ and $V(\mathbf{r}) = \frac{\nabla^2}{2}$. The Kohn-Sham equation reads:

$$\left[-\frac{\nabla}{2} + V_{\mathrm{eff}}(\mathbf{r})\right]\psi_\mu(\mathbf{r}) = E_\mu(\mathbf{r})\psi_\mu(\mathbf{r}), \quad E_1 \leq E_2 \leq ... \tag{2.23}$$

and is solved by determining the N_{El} energetically lowest eigenstates of the system of non-interacting particles. Consequently, by inserting the wavefunctions into the given $V_{\mathrm{eff}}(\mathbf{r})$, the energies can be obtained. These equations are self-consistent and must be solved iteratively until convergence is reached. However, the exact form of V_{XC} is unknown, so this potential is approximated using the local density approximation (LDA) or the Generalized Gradient-Approximation (GGA).

The density follows from the Kohn-Sham orbitals as $n(\mathbf{r}) = \sum_i \gamma_\mu |\psi_\mu(\mathbf{r})|^2$, where

$$\gamma_\mu = \begin{cases} 1 : E_\mu < \kappa \\ 0 \leq \gamma_\mu \leq 1 : E_\mu = \kappa, \quad \kappa\text{...chem. potential} \\ 0 : E_\mu > \kappa \end{cases} \tag{2.24}$$

2.1.5 Bloch Theorem

After deriving an efficient algorithm for energy minimization, we now turn to calculations of macroscopic crystals. Even a system of just one cubic millimeter already contains on the order of 10^{20} particles. Handling such a large number of particles requires substantial computational time. Most crystalline systems are arranged in a periodic lattice. This periodicity can be exploited to reduce both complexity and runtime.

First, periodic systems satisfy the periodic boundary condition: $V(\mathbf{r}) = V(\mathbf{r}+\mathbf{R})$, where $\mathbf{R} = n_1\mathbf{a}_1 + n_2\mathbf{a}_2 + n_3\mathbf{a}_3$ is the lattice vector. Bloch's theorem now states that the eigenfunctions of the orthonormal set of Bloch states can be chosen to satisfy the Bloch property, i.e. under translation by a reciprocal lattice vector $\mathbf{G} = n_1\mathbf{b}_1 + n_2\mathbf{b}_2 + n_3\mathbf{b}_3$ with $\mathbf{b_i} \cdot \mathbf{a_j} = 2\pi\delta_{ij}$ they change by a phase factor:

$$\psi(\mathbf{r}+\mathbf{R}) = e^{i\mathbf{k}\cdot\mathbf{R}}\psi(\mathbf{r}), \tag{2.25}$$

where $\mathbf{k}$ is a wavevector in the first Brillouin zone. We now define a lattice-periodic function $u(\mathbf{r}) = u(\mathbf{r}+\mathbf{R})$ such that $\psi(\mathbf{r}) = e^{i\mathbf{k}\cdot\mathbf{r}}u(\mathbf{r})$. Then the eigenfunctions can be written in the form [5]:

$$\psi_{\mu,\mathbf{k}}(\mathbf{r}) := \psi_\mu(\mathbf{k},\mathbf{r}) = e^{i\mathbf{k}\cdot\mathbf{r}}u_\mu(\mathbf{k},\mathbf{r}) \tag{2.26}$$

If we now extend the system to N_p cells, each with reciprocal-cell volume $\Omega_p = \det(\mathbf{b_1}, \mathbf{b_2}, \mathbf{b_3})$, the eigenfunctions can be expanded in a Fourier series as:

$$\psi_{\mu,\mathbf{k}}(\mathbf{r}) = \frac{1}{\sqrt{N_p\Omega_p}}\sum_{\mathbf{G}} c_{\mu,\mathbf{k}}(\mathbf{G})e^{i(\mathbf{k}+\mathbf{G})\cdot\mathbf{r}}, \tag{2.27}$$

where $c_{\mu,\mathbf{k}}(\mathbf{G})$ are the coefficients of the plane waves. In calculations, the eigenfunctions are evaluated on a finite set of $\mathbf{k}$-points, producing a discrete set of eigenstates. In the limit of an infinitely dense grid, the eigenvalues $E_{\mu,\mathbf{k}}$ form continuous energy bands. The Kohn-Sham equation in reciprocal space becomes:

$$\sum_{G'}\left[\frac{|\mathbf{k}+\mathbf{G}|^2}{2}\delta_{\mathbf{G},\mathbf{G}'} + V_{\mathrm{KS}}[n](\mathbf{G}-\mathbf{G}')\right]c_{\mu,\mathbf{k}}(\mathbf{G}') = E_{\mu,\mathbf{k}}c_{\mu,\mathbf{k}}(\mathbf{G}) \tag{2.28}$$

For practical calculations, a cutoff for the kinetic energy is introduced to limit the plane-wave expansion. Only reciprocal lattice vectors $\mathbf{G}$ satisfying the condition:

$$\frac{|\mathbf{k}+\mathbf{G}|^2}{2} \leq E_{\mathrm{cut}} \tag{2.29}$$

This limits the number of plane waves used and thus reduces computational cost. Both the kinetic energy cutoff and the density of the k-point mesh must be chosen carefully to ensure a well-converged and accurate description of the electronic structure.

2.2 Bandstructure interpolation with Wannier functions

Wannier functions form an orthonormal, localized basis set for periodic solids. Formally, they come as the Fourier transform of the Bloch states:

$$w_{\mu,\mathbf{R}}(\mathbf{r}) = \frac{V}{(2\pi)^3} \int_{\mathrm{BZ}} e^{-i\mathbf{k}\cdot\mathbf{R}}\, \psi_{\mu,\mathbf{k}}(\mathbf{r})\ \mathrm{d}\mathbf{k}\ , \tag{2.30}$$

where $\psi_{\mu,\mathbf{k}}(\mathbf{r}) = e^{i\mathbf{k}\cdot\mathbf{r}} u_{\mu,\mathbf{k}}(\mathbf{r})$ are the Bloch orbitals. By a suitable k-dependent choice of phase (gauge), the Wannier functions can be shaped to be maximally localized. For the construction of maximally localized Wannier functions (MLWF), the spread functional is defined as

$$\Omega = \sum_n \Big[\langle w_{n0}|\mathbf{r}^2|w_{n0}\rangle - \langle w_{n0}|\mathbf{r}|w_{n0}\rangle^2 \Big] \tag{2.31}$$

and minimized via unitary transformations within the chosen subset of bands. The minimization procedure consists of a disentanglement step (separating the relevant bands) followed by a localization optimization using gradient-based methods. From the MLWF one obtains the effective tight-binding Hamiltonian in real space

$$H_{mn}(\mathbf{R}) = \langle w_{m0}|\hat{H}|w_{n,\mathbf{R}}\rangle\, , \tag{2.32}$$

which retains only hopping matrix elements beyond a certain distance. This compact model reproduces the DFT bands exactly within the specified energy window. Using a Fourier transform

$$H_{mn}(\mathbf{k}) = \sum_{\mathbf{R}} e^{i\mathbf{k}\cdot\mathbf{R}}\, H_{mn}(\mathbf{R}) \tag{2.33}$$

the interpolated Hamiltonian matrices emerge on arbitrarily fine k-grids. The diagonalization produces high-resolution band structures, Fermi surfaces, and topological invariants, without performing additional DFT-computationally intensive self-consistent runs. This procedure is particularly effective for detecting subtle topological features such as WPs or Fermi arcs, as it enables an exact reproduction of the DFT results with minimal computational effort on dense k-meshes.

2.3 Lattice dynamics and DFPT

DFPT is a linear response formalism within density functional theory that responds to infinitesimal perturbations of the crystal lattice, an electric field, or other external potentials. Instead of computing excited many-electron states in full, one uses the first-order variation of the Kohn-Sham equations. This allows to gain lattice dynamics, electric susceptibilities, and phonons efficiently without costly supercell calculations [16].
A perturbation of the system can be described by the first-order Sternheimer equation:

$$\left(\hat{H}^{(0)} - E_\mu^{(0)}\right) \psi_\mu^{(1)} = -\left(U^{(1)} - E_\mu^{(1)}\right) \psi_\mu^{(0)}. \tag{2.34}$$

with $U := V_{\text{eff}}$. Small displacements $\mathbf{u}_I$ of the atoms from their equilibrium positions $\mathbf{R}_I$ lead to a perturbation of the effective potential:

$$U(\{\mathbf{R}_I\}) \to U(\{\mathbf{R}_I\} + \{\mathbf{u}_I\}). \tag{2.35}$$

The variation in the potential can be very complex, therefore the potential is approximated by a Taylor series expansion:

$$U(\{\mathbf{R}_I\} + \{\mathbf{u}_I\}) = U(\{\mathbf{R}_I\}) \tag{2.36}$$

$$+ \sum_{I=1}^{N_{\text{Ion}}} \left.\frac{\partial U}{\partial \mathbf{u}_I}\right|_{\mathbf{u}_I=0} \mathbf{u}_I \tag{2.37}$$

$$+\frac{1}{2} \sum_{I,J=1}^{N_{\text{Ion}}} \left.\frac{\partial^2 U}{\partial \mathbf{u}_I \partial \mathbf{u}_J}\right|_{\mathbf{u}_I=0} \mathbf{u}_I \mathbf{u}_J \tag{2.38}$$

$$+... \tag{2.39}$$

The first-order term vanishes at equilibrium. Define $\Phi_{IJ} := \left.\frac{\partial^2 U}{\partial \mathbf{u}_I \partial \mathbf{u}_J}\right|_{\mathbf{u}_I=0}$. We thus obtain an equation of motion for the lattice vibrations:

$$M_I \ddot{\mathbf{u}}_I = -\frac{\partial U(\{\mathbf{u}\})}{\partial \mathbf{u}_I} = -\frac{\partial}{\partial \mathbf{u}_I} \left[U_0 + \frac{1}{2} \sum_{I,J=1}^{N_{\text{Ion}}} \Phi_{IJ} \mathbf{u}_I \mathbf{u}_J \right] = \sum_{J=1}^{N_{\text{Ion}}} \Phi_{IJ} \mathbf{u}_J \tag{2.40}$$

We write the displacement in Bloch form over the wavevectors $q = \frac{2\pi}{\lambda} = \frac{2\pi}{N_{Ion} \cdot a/I}$ where a is the 1D lattice vector:

$$\mathbf{u}_I = \mathbf{u}_q e^{iq\mathbf{R}_I} e^{-i\omega_q t} \tag{2.41}$$

where ω_q and $\mathbf{u}_q$ are the phonon frequency and eigenvector, respectively. For the equation of motion it follows:

$$M\omega_q^2\mathbf{u}_q = \sum_{J=1}^{N_{\mathrm{Ion}}} \Phi_{IJ}\,\mathbf{u}_q\,e^{iq(\mathbf{R}_J-\mathbf{R}_I)}. \tag{2.42}$$

We thus obtain the dynamical matrix:

$$D_{IJ}(q) = \frac{1}{M}\sum_{J=1}^{N_{\mathrm{Ion}}} \Phi_{IJ}\,e^{iq(\mathbf{R}_J-\mathbf{R}_I)}. \tag{2.43}$$

With this matrix the secular equation can be solved to obtain the frequencies:

$$[D(q)-\omega_q^2]\mathbf{u}_q = 0 \Rightarrow \omega_q^2 = D(q) \tag{2.44}$$

The dynamical matrix can be extended to three dimensions and N_p cells:

$$D(\mathbf{q}) = \sum_{\kappa\alpha p} \frac{\Phi_{\kappa\alpha p,\kappa'\alpha' p'}}{\sqrt{M_\kappa M_{\kappa'}}} e^{i\mathbf{q}(\mathbf{R}_p-\mathbf{R}_{p'})} \tag{2.45}$$

where κ is the atom index, p the cell index, and α the Cartesian coordinate.

2.4 Spin-Orbit-Coupling

The SOC arises from the relativistic interaction between the spin of an electron and the effective magnetic field that the electron experiences due to its Coulomb motion around the nucleus.

SOC lifts spin degeneracies in bands, especially in heavy atoms, and leads to characteristic band shifts and splittings. In crystalline systems without an inversion center—such as in the T_d phase of MoTe$_2$ — SOC can produce point-like band touchings: two degenerate bands with opposite spin projections split, leaving isolated WPs near the Fermi level.

2.5 Topological bandtheory and Weyl-Fermions

2.5.1 Weyl equation

Weyl fermions are massless quasiparticles that derive from the linear Weyl equation and appear in solids as point-like band touchings in momentum space. Each of these points, so-called Weyl-Points, carries a well-defined chirality, which as a topological invariant describes the flux of Berry curvature. The existence of WP requires the breaking of either inversion or time-reversal symmetry in the crystal.

The effective Hamilton operator near a WP reads [50]

$$H_\chi(\mathbf{k}) = \hbar v_F \, \sigma \cdot (\mathbf{k} - \mathbf{k}_0) \, ,$$

where v_F denotes the Fermi velocity, σ the Pauli matrices, and $\chi = \pm 1$ the chirality. The dispersion $E_\pm(\mathbf{q}) = \pm \hbar v_F |\mathbf{q}|$ forms two conical bands that touch exactly at the point $\mathbf{k}_0$.

The chirality can be computed via the Chern number of a small sphere S around the node [48]:

$$C_\chi = \frac{1}{2\pi} \oint_S \mathbf{\Omega}(\mathbf{k}) \cdot d\mathbf{S} = \chi \, ,$$

where the Berry curvature [4] $\mathbf{\Omega}(\mathbf{k}) = \nabla_\mathbf{k} \times \langle u_\mathbf{k} | i \nabla_\mathbf{k} | u_\mathbf{k} \rangle$ describes the local geometric structure of the wavefunctions.

Topologically induced Fermi arcs connect, on the surface of a WSM, projections of Weyl pairs of opposite chirality. In the bulk of the material these pairs always appear in pairs to balance the total chirality. WSMs can be classified into Type I and Type II [43]:

- Type I features upright Weyl cones and point-like Fermi surfaces.
- Type II shows strongly tilted cones with adjacent electron and hole pockets

This classification influences transport phenomena such as the chiral anomaly effect and negative magnetoresistance.

2.6 Phonon theory and atom displacement

In the harmonic approximation model of a crystal, all N_p unit cells and their atoms perform small oscillations around the equilibrium positions $\mathbf{R}_p$. These collective vibrations can be described as a superposition of normal modes. Each mode $(\mathbf{q}, \nu)$ has a characteristic frequency $\omega_{\mathbf{q}\nu}$ and a polarization vector $e_\kappa^\nu(\mathbf{q})$ for atom κ. The quantized displacement of atom κ in cell p is expressed by the operator [10]:

$$\Delta \hat{\tau}_{\kappa p} = \sqrt{\frac{M_0}{N_p \, M_\kappa}} \sum_{\mathbf{q},\nu} e^{\, i\mathbf{q}\cdot\mathbf{R}_p} \, e_\kappa^\nu(\mathbf{q}) \, l_{\mathbf{q}\nu} \, \hat{Q}_{\mathbf{q}\nu} . \tag{2.46}$$

Here are:

- M_0 is a reference mass, often the proton mass, and M_κ is the mass of atom κ.
- The factor $1/\sqrt{N_p}$ ensures normalization over all cells.
- $e_\kappa^\nu(\mathbf{q})$ describes the relative motion of atom κ in mode ν.
- $l_{\mathbf{q}\nu} = \sqrt{\hbar/(2M_0\omega_{\mathbf{q}\nu})}$ is the zero-point amplitude.
- $\hat{Q}_{\mathbf{q}\nu}$ is the phononic normal-coordinate operator, which is linked to the annihilation and creation operators $b_{\mathbf{q}\nu}$, $b^\dagger_{-\mathbf{q}\nu}$.

When a strong optical field or an ultrafast laser pulse is applied to the lattice, this field acts on the electrons and shifts their occupation density. Through the electron-phonon interaction, this change in populations generates a nonzero expectation value $\langle Q_{\mathbf{q}\nu}(t)\rangle$ in eq. (2.46). For coherent excitation at $\mathbf{q} = 0$ one obtains a collective mode displacement

$$\Delta\tau_{\kappa p}(t) = \sqrt{\frac{M_0}{N_p M_\kappa}} \sum_\nu e_\kappa^\nu(0)\, l_{0\nu}\, \langle Q_{0\nu}(t)\rangle\,, \tag{2.47}$$

which in real time manifests as an oscillatory shear or stretch motion of the lattice. In materials like T_d-MoTe$_2$ such a shear motion may suffice to shift the lattice over a phase barrier into the centrosymmetric $1T'$ phase, thereby triggering an ultrafast phase-transition (PT).

3 Methods

The methods section focuses on the use of open-source software and the fine-tuning of relevant parameters to carry out theoretically founded simulations. Familiarization with the chosen software required several weeks, as a deep understanding of its functions and capabilities had first to be developed. During the course of the work, alternative programs were repeatedly considered to achieve broader or more precise results. However, due to the time and organizational constraints of a bachelor's thesis, implementation of additional software tools was not feasible. The selection and scope of the methods employed are therefore deliberately limited to an appropriate level due to the format of this academic work.

3.1 Software workflow

To obtain the results, a selection of open-source software was used. In the first step, Quantum ESPRESSO (QE) [16, 15] was used to compute the stable phases as well as the electronic band structures of $\mathrm{MoTe_2}$. Furthermore, this software enabled the analysis of coherent phonon vibrational modes. For the interpolation of the calculated band structures, Wannier90 (W90) [38] was subsequently applied. For visualization and analysis of the crystallographic and electronic data, I used *Python, VESTA, Bilbao Crystallographic Server* [33, 47, 2, 1] as well as *SeekPath* [21, 49].

3.1.1 Quantum Espresso

Quantum ESPRESSO (*opEnSource Package for Research in Electronic Structure, Simulation and Optimization*) is an open-access software suite for computing the electronic structure of materials at the atomic scale. It is based on DFT and employs plane waves and pseudopotentials to determine physical properties such as total energy, band structure, density of states, and phonon dispersion relations. The software is suitable for both periodic solids and isolated systems modeled via supercells.

The calculations are controlled via so-called input files, in which the material structure, the type of calculation, and various parameters such as lattice constants, atomic positions, and the k-point grid are specified. The selection of pseudopotentials as well as the exchange-correlation functionals is also done there. Two central parameters that are particularly important for reliable results are the cutoff energy and the fineness of the k-point mesh - both require convergence testing. Depending on the system, additional effects such as SOC, special crystal symmetries, or smearing of the electronic states above the Fermi level can be taken into account.

QE consists of multiple modules, including “PWscf” for the self-consistent solution of the Kohn-Sham equations, “PHonon” for the calculation of lattice dynamics via DFPT, and “PostProc” for the analysis and graphical presentation of results. The package is optimized for high-performance computing environments and supports both MPI and OpenMP parallelization, making it particularly powerful for large-scale simulations.

3.1.2 Wannier90

Wannier90 is an open-source software specialized in generating localized, orthonormal Wannier functions from the delocalized Bloch states of periodic DFT calculations. These maximally localized orbitals constitute a compact basis set that is well suited for various post-processing tasks - from high-resolution band structure interpolation and precise Fermi-surface representations to Berry phase and electronic transport property calculations.

In essence, W90 operates in two stages: first, it reads the overlap matrices and projections required for the process from any DFT-code. Subsequently, an optimization algorithm performs a unitary transformation that minimizes the spatial extent of the orbitals, thus “contracting” the Wannier functions. The result of this procedure is a set of localized orbitals whose Hamiltonian matrix elements in the Wannier basis are stored.

The generated localized orbitals not only enable fast and accurate reconstruction of electronic properties, but are also suitable for investigating complex effects such as band disentanglement, spin-orbit effects, and topological invariants.

3.1.3 Other software

Python is an object-oriented programming language with numerous libraries for data analysis and plotting, notably xarray, numpy, and matplotlib.

VESTA is a tool for visualizing crystal structures, electron densities, and isosurfaces.

SeekPath is a web-based utility that, among other functions, uses QE input files

Table 3.1: exp. cell parameters of $MoTe_2$

	$T_{d,exp}$	$1T'_{exp}$
a_1 in a_0	6.6254	6.5555
a_2 in a_0	12.0187	11.9620
a_3 in a_0	25.9762	26.1916
$\alpha := \arcsin\left(\frac{a_2}{a_3}\right)$ in $\circ$	90.00	92.12
cell type	orthorhombic	monoclinic

Table 3.2: exp. atom positions of $MoTe_2$ in crystal coordinates

	$T_{d,exp}$	$T_{d,exp}$	$T_{d,exp}$	$T_{d,exp}$	$1T'_{exp}$	$1T'_{exp}$	$1T'_{exp}$	$1T'_{exp}$
Atom	Wyckoff	x	y	z	Wyckoff	x	y	z
Mo_1	2a	0.0	0.6052	0.5003	2e	0.25	0.1833	0.0074
Mo_2	2a	0.0	0.0301	0.0147	2e	-0.25	0.3181	0.5066
Te_1	2a	0.0	0.8626	0.6557	2e	0.25	0.5888	0.1045
Te_2	2a	0.0	0.6405	0.1125	2e	-0.25	0.0970	0.1486
Te_3	2a	0.0	0.2900	0.8593	2e	-0.25	0.5568	0.3516
Te_4	2a	0.0	0.2160	0.4027	2e	0.25	0.0563	0.3955

to determine an optimal path covering the entire Brillouin zone.
Bilbao Crystallographic Server provides web-based tools for symmetry analysis, space-group determination, and visualization of irreducible representations.

3.2 Computing structure

$MoTe_2$ is a widely studied material. On the Materials Project website [27], the atomic structures of the T_d- and $1T'$-phases can be found. Even from the coordinates given in table 3.2, one can observe that symmetry prevails in these phases. Comparison with [7] revealed no deviation from the reported parameters. The unit cells of the phases in table 3.1 (lattice parameters in $a_0 = \frac{4\pi\epsilon_0\hbar^2}{e^2 m_e} \approx 0.5292\text{Å}$) are of similar size and indicate an orthorhombic and a monoclinic structure, respectively.

To find the most energetically favorable unit cell and atomic positions, the isolated system should have vanishing forces. To achieve this, a relaxation calculation was performed in QE. For this calculation, a maximum pressure threshold of 0.1 kBar was set. The unit cell was allowed to adjust its lattice parameters while preserving the cell types (orthorhombic and monoclinic). The atoms were constrained to move only within the yz-plane. Furthermore, the corresponding space group was

specified so that QE could exploit the symmetry for simpler computations. The cell and atomic relaxations were carried out using the standard BFGS algorithm (quasi-Newton method).
I obtained the pseudopotentials from the QE library according to the following criteria: high accuracy (Projector Augmented-Wave (PAW)), solid-state crystal (PBEsol (GGA functional)), relativistic with spin (full relativistic).
The cutoff energy (80 Ry), smearing (gauss: 4.5 mRy) and k-point grid ($19 \times 11 \times 5$) were used for the relaxation only after the convergence tests in section 3.3.
In layered materials such as $MoTe_2$, (VdW) interactions play a crucial role, so these dispersions were additionally accounted for using Grimme's DFT-D3 method [18]. To assess the impact of the VdW correction on the electronic structure, all calculations - especially the band structure comparisons - were repeated both with and without the DFT-D3 correction. In parallel, SOC was explicitly enabled in all input files, as it has significant effects on the band dispersion and band gaps in TMDs.

3.3 Parameter selection

To enable an approximately equidistant sampling, I calculated the necessary k-points for sampling n_{k,a_1} in the a_1-direction, n_{k,a_2} in the a_2-direction, and n_{k,a_3} in the a_3-direction based on the lattice constants:

$$\begin{aligned} n_{k,a_2} &= \frac{a_2}{a_1} \cdot n_{k,a_1} \approx 1.8 \cdot n_{k,a_1} \\ n_{k,a_3} &= \frac{a_3}{a_1} \cdot n_{k,a_1} \approx 3.9 \cdot n_{k,a_1} \end{aligned}$$

Accordingly, we obtain grids of values as shown in table 3.3. During the convergence test of the k-point grids, a cutoff of 80 Ry was adopted.

To determine a suitable cutoff energy, systematic convergence tests were carried out in the range from 0 to 140 Ry with a step size of 10 Ry. A fixed k-point grid of $20 \times 11 \times 5$ was used. The calculations revealed that the computation time increased steeply with higher cutoff energies, owing to the exponential growth of numerical complexity. For this reason, no further Self-Consistent Field (SCF) calculations beyond 140 Ry were performed, as their practical execution with acceptable resource demands no longer appeared feasible. The aim was to identify the lowest possible cutoff energy that still provides a numerically stable basis for all subsequent calculations.

Table 3.3: Calculated k-point samplings for convergence test

$n_{k,a_1} \times n_{k,a_2} \times n_{k,a_3}$	n_k	$n_{k,a_1} \times n_{k,a_2} \times n_{k,a_3}$	n_k
2 × 1 × 1	2	3 × 2 × 1	6
4 × 2 × 1	8	5 × 3 × 1	15
6 × 3 × 2	36	7 × 4 × 2	56
8 × 4 × 2	64	9 × 5 × 2	90
10 × 6 × 3	180	11 × 6 × 3	198
12 × 7 × 3	252	13 × 7 × 3	273
14 × 8 × 4	448	15 × 8 × 4	480
16 × 9 × 4	576	17 × 9 × 4	612
18 × 10 × 5	900	19 × 11 × 5	1045
20 × 11 × 5	1100	21 × 12 × 5	1260
22 × 12 × 6	1584	23 × 13 × 6	1794
24 × 13 × 6	1872	25 × 14 × 6	2100
26 × 14 × 7	2548	27 × 15 × 7	2835
28 × 16 × 7	3136	29 × 16 × 7	3248

To select an appropriate smearing value, the Gaussian distribution (gaussian spreading) as implemented in the QE standard was used. The test series began at a smearing value of 0 Ry, sampling initially in fine increments of 0.5 mRy to probe the system's response to minimal thermal broadening. From 15 mRy onward, sampling proceeded in coarser steps of 10 mRy. The objective of this tiered approach was to identify the smallest smearing value that still enables numerically stable self-consistency without unnecessarily broadening electronic states.

3.4 Computing Bandstructure

To visualize the high-symmetry points within the Brillouin zone of the T_d phase of $MoTe_2$, the Bilbao Crystallographic Server was used. The graphical depiction of these points is shown in fig. 3.1. Based on this information, an appropriate k-path for the band-structure calculation was determined using the SeekPath tool: Γ-X-S-Y-Γ-Z-U-R-T-Z|Y-T|U-X|S-R. This choice of path enables a comprehensive analysis of the electronic structure along the principal symmetry lines.

For the band structure, both SCF and Non-Self-Consistent Field (NSCF) calculations were performed. The basis was the previously optimized lattice parameters from the relaxation and convergence tests for both crystallographic phases. The chosen path was sampled with a high resolution of 50 points per segment. The SCF calculation included all 136 electronic bands described by the system.

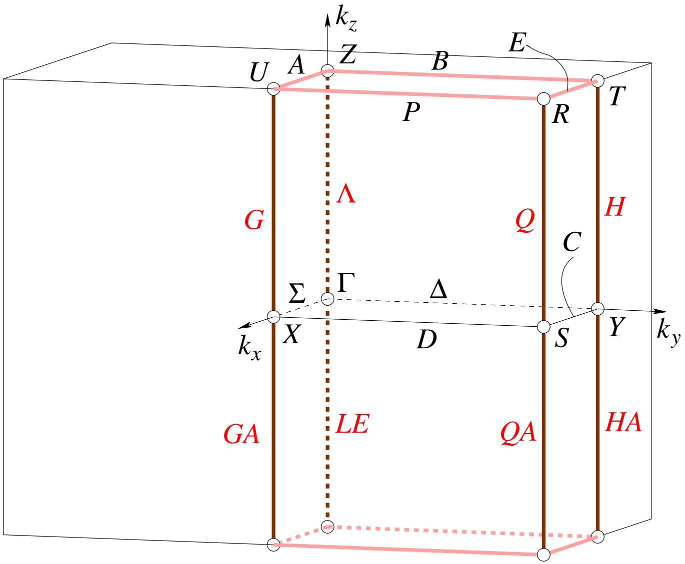

©bilbao crystallographic server
http://www.cryst.ehu.es

Figure 3.1: Brillouin zone of space group $Pmn2_1$ with high-symmetry paths

For further refinement of the band structure representation, interpolation using W90 was performed. The same parameters as in the previous calculations were used to ensure comparability of the results. For the interpolation, an energy range from 4 eV to 15 eV was defined, considering the upper 88 bands. The k-point grid of the preceding NSCF calculation had a resolution of $24 \times 12 \times 8$. The final interpolation of the band structure was performed with W90 both along the chosen path and across the k_x-k_y plane of the Brillouin zone. The grid points in this plane were sampled with a spatial resolution of $\frac{2.5 \cdot 10^{-3}}{b_i}$, where $b_i \in \{b_2, b_3\}$ denote the corresponding reciprocal lattice vectors.

3.5 Computing Phonons

For the calculation of the phonon dispersion, an SCF calculation was first performed using a $12 \times 7 \times 5$ k-point grid. This grid provided a practical compromise between computational accuracy and time required, enabling the lattice vibration simulation to be completed within approximately one month.

The subsequent phonon calculation was carried out on a q-point grid with resolution $5 \times 3 \times 2$, which defines the sampling density in the Brillouin zone for lattice vibrations. The resulting phonon modes were obtained as eigenvectors and then converted into real atomic displacements according to eq. (2.46). These displacement vectors were subsequently added, in multiples, to the atomic configuration of the T_d phase of $MoTe_2$ to generate the distorted structures for further analysis.

3.5.1 Computing phase transition

In the next step, targeted atomic displacements were applied in an attempt to induce a structural PT. The modified atomic positions were then evaluated for their membership in a specific space group. The criterion for success was the transition to the space group $P2_1$, which was taken as an indicator of the formation of a new crystalline phase.

Subsequently, a relaxation of the displaced configurations was performed to evaluate their structural stability and verify them energetically. The magnitude of each displacement was defined as the average distance from the original atomic position. In this investigation, mode-based displacements in the range from 0 Å to 3 Å with a step size of 0.1 Å were applied and analyzed with respect to their effects on the space group.

To classify the resulting space group after each displacement, the displaced atomic positions were systematically mapped into the unit cell of the $1T'$ phase. This ensures a consistent basis for comparison within the crystallographic framework and enables a clear view of the phase behavior.

4 Results

The results of this work are divided into four sections. First, the convergence studies are presented. Here, three parameters were tested to enable a stable and as time-efficient calculation as possible. Subsequently, an overview of the resulting band structures is provided. These were presented both along high-symmetry paths through reciprocal space and in the k_x-k_y plane. Here, the WPs can be clearly identified in various views.
In the next chapter, the results of the phonon calculations are presented. A phonon dispersion along various high-symmetry paths provides insight into the validity of the results. Furthermore, the associated phonon motions at the Γ-point are shown based on selected modes. Finally, possible PTs via linear combinations of different modes are introduced.

4.1 Convergence studies

In the convergence studies, the parameters E_{cut}, k-point density, and smearing were systematically varied and their impact on the total energy was investigated. For better comparability, all plots display the relative deviation of the minimum total energy on the y-axis, while the tested parameters form the x-axis.
The presentation of the E_{cut}-plot is in linear scaling, as the energy evolution with respect to this parameter is comparatively continuous. In contrast, logarithmic scales were used on the x-axis for the diagrams of k-points and smearing to better reveal the strongly nonlinear effects at low-value ranges. In all three cases, the transition to the respective energy minimum is highlighted by two diagonal lines on the y-axis, marking a sudden drop and thereby point out the convergence.

4.1.1 Convergence of total energy

The convergence of the total energy as a function of the cutoff energy is shown in fig. 4.1, illustrated for two different k-point grids with 240 and 3136 points, respectively. Both curves exhibit a clearly visible exponential decay of the energy with

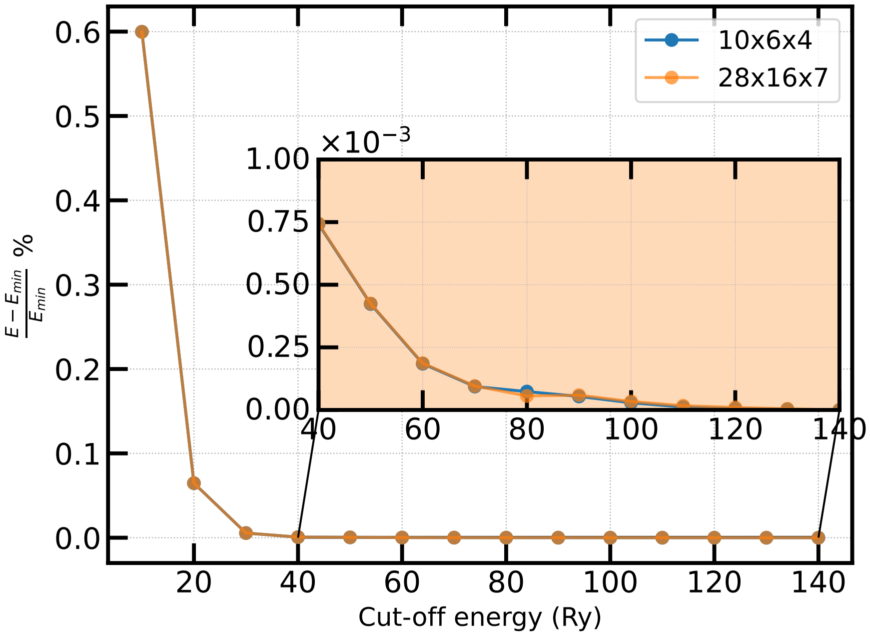

Figure 4.1: Convergence of E_{tot} at $E_{\text{cut}} = 80$ Ry

increasing cutoff, with the maximum value at 0 Ry being approximately 0.6% above the energetic minimum at 140 Ry.

A magnified inset of the curve reveals that already at a cutoff energy of 80 Ry a deviation of merely 10^{-4} % from the minimum value is achieved. This difference lies well below the chosen significance threshold, so no relevant numerical advantages are to be expected from any further increase in the cutoff energy. For reasons of computational economy, 80 Ry was therefore adopted as the cutoff energy for all subsequent calculations.

4.1.2 Convergence of k-points

The convergence study in fig. 4.2 focuses on the number of k-points and their impact on the total energy. In contrast to the cutoff energy, no clearly exponential decrease can be observed here. A rough convergence trend becomes noticeable already above a certain threshold n_{k,a_1}, but only in the zoomed inset does true energetic stabilization emerge at about $n_{k,a_1} = 18$.

Since the k-point parameter significantly contributes to the precision of the DFT calculation and simultaneously affects all subsequent simulations, a k-point grid of $20 \times 11 \times 5$ was chosen for standard calculations. For particularly sensitive or high-resolution calculations, the sampling was further increased to a grid of $28 \times 16 \times 7$

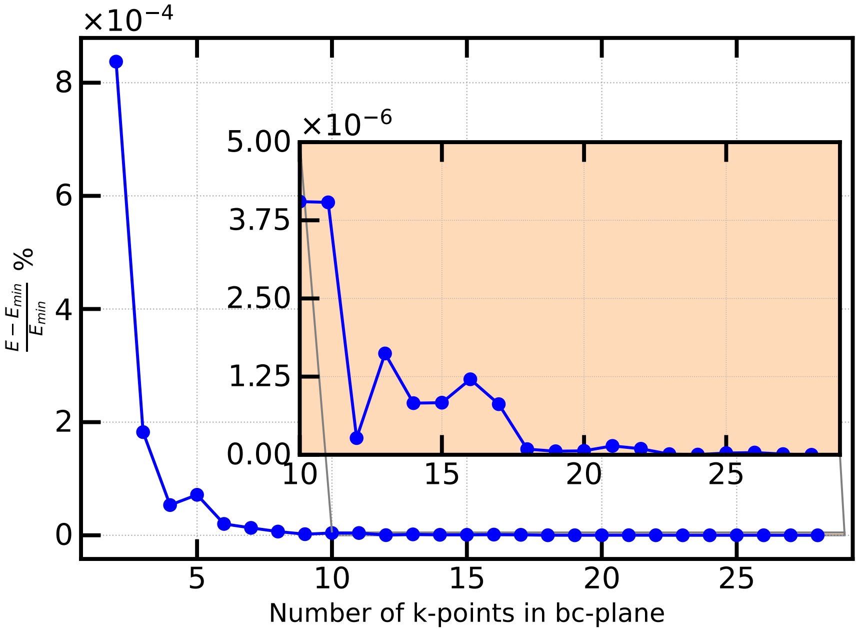

Figure 4.2: Convergence of E_{tot} at $n_{k,a_1} = 18$

to ensure maximum computational accuracy.

4.1.3 Smearing convergence

The final convergence test focuses on selecting an appropriate smearing parameter, which in DFT calculations is used for the thermal broadening of the electronic occupation function. A differentiated sampling was performed: in the critical range between 0 mRy and 15 mRy, fine-grained sampling in small increments was applied, while in the higher range from 20 mRy to 60 mRy, computations were carried out in 10 mRy steps.

fig. 4.3 shows a typical exponential decay of the total energy as a function of the smearing value. The curve is initially flat before the slope increases significantly at around 60 mRy, indicating growing energetic distortion due to excessive smearing. While a high smearing value can promote numerical stability, it leads to undesired smoothing of the band structure and thus to a loss of physical significance. On the contrary, a too low value can lead to instability of the self-consistency.
A finer analysis shows that below 4.5 mRy no significant improvement in the energy deviation occurs, as the difference from the initial value falls below 10^{-5} Ry and thus lies under the defined threshold for numerical relevance. For this reason, 4.5

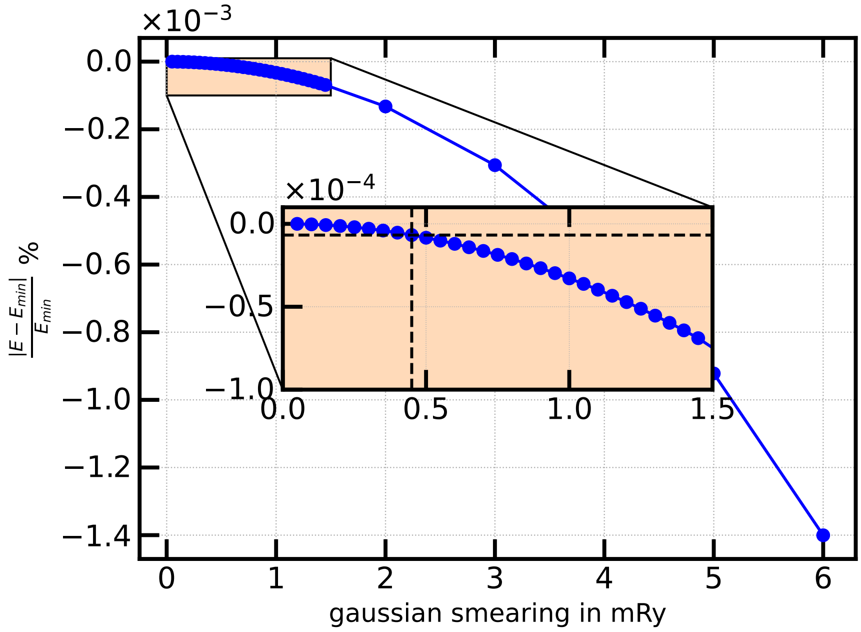

Figure 4.3: Convergence of E_{tot} at $\sigma = 4.5$ mRy

mRy was chosen as the optimal smearing value for all further calculations.

4.1.4 Crystal structure

With the parameters from section 3.3 and those from the convergence studies, a VC-relax was performed for both phases. This resulted in a change of the respective cell by a few Å as shown in table 4.1. The atomic positions moved on average by about 4 mÅ due to the relaxation. The atomic structure in the yz-plane is depicted in fig. 4.4. The atoms and respective phases are color-distinguishable (see caption). In the figure at the origin, the unit cells with their 4 Mo and 8 Te atoms are shown. It is noticeable that there are no major differences between the phases within the unit cells. Upon closer inspection, an intralayer shear of the Te atoms around the Mo atoms in the b direction can be observed. Also, further layers are depicted. In fig. 4.4, the interlayer shear is clearly visible.

4.2 Band structure

After the structures were clearly defined, the band structures were calculated. First, band structures were computed along a high-symmetry path in the Brillouin zone.

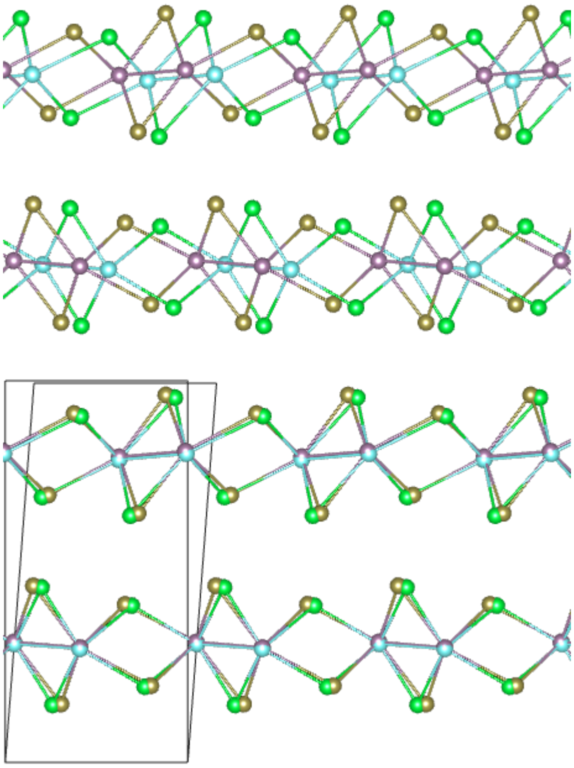

Figure 4.4: T_d- and $1T'$-phase overlay;$1T'$-phase holds intra- and interlayer shift in y-direction compared to T_d-phase

Table 4.1: exp. vs. sim. cell parameters of $MoTe_2$

	$T_{d,exp}$	$T_{d,rel}$	$1T'_{exp}$	$1T'_{rel}$
a_1 in a_0	6.6254	6.5184	6.5555	6.5213
a_2 in a_0	12.0187	11.9205	11.9620	11.9317
a_3 in a_0	25.9762	24.9900	26.1916	24.9869
α in $\circ$	90	90	92.12	94.32

For higher resolution, these were interpolated using W90. Also, a comparison of the band structures with and without VdW correction is presented.

In addition to the representation along a path, the bands near the Fermi energy were plotted in the k_x-k_y plane. Within the difference between the nearest valence and conduction bands, WPs become visible. The band structure along the path between the WPs is shown additionally.

4.2.1 High-symmetry path

For better comparability, the band structures in fig. 4.5 of both phases were calculated along the same path. The computed Fermi energy is $E_F = 10.855\,\mathrm{eV}$. On the y-axis, the energy minus the Fermi energy is plotted. The x-axis displays the symmetry points. The band structures along the path Γ-X-S-Y-Γ-Z-U-R-T-Z|Y-T|U-X|S-R show dense valence and conduction bands near the Γ point, while at the edges of the Brillouin zone band gaps of up to 2 eV are visible.

At first glance, the band structures appear very similar. In the zoom between Γ and X, the SOC of the T_d phase becomes evident, with the bands lying within a few tens of meV of each other. In this region, the WPs also become visible in further results. In the $1T'$ phase, however, no SOC is observed, and the bands are more widely separated.

fig. 4.6 shows the difference between a band structure calculated with and without VdW correction along the path Γ-X. Here, in particular in the valence bands, offsets of about 100 meV are visible. The contribution from the VdW correction can thus make a significant difference for such fine-grained calculations.

Upon closer inspection of the zoom into the band structure of the T_d phase in fig. 4.7, a high grid resolution is necessary to ensure the visibility of band crossings when adjacent bands approach each other. Although this is possible with pure DFT calculations, it requires extensive computation time due to the large number of grid points. Using W90, the DFT calculations could be interpolated. As shown in fig. 4.7, these interpolations were very successful, and for further descriptions of the band structures only data interpolated with W90 were used.

4.2.2 k_x-k_y-plane

After comparing the band structure along the path with other results in section 5.1, the band structure in the k_x-k_y plane was examined for WPs, and in the end, two

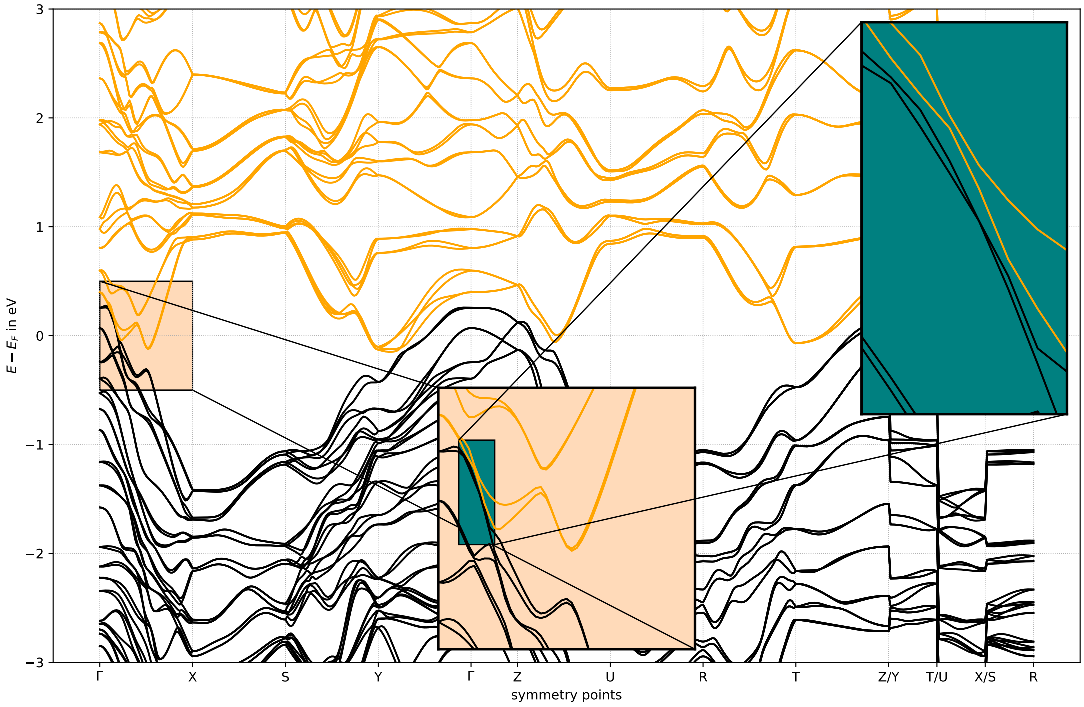

(a) Bandstructure of T_d-MoTe$_2$ via DFT shows close bands near E_F due to SOC

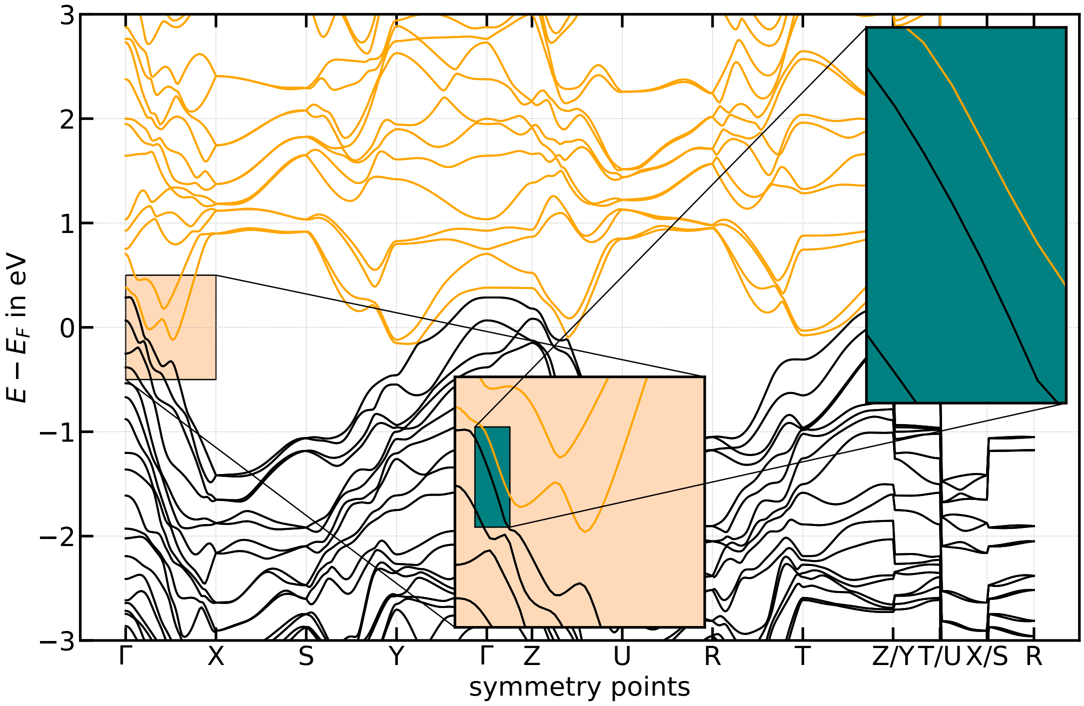

(b) Bandstructure of $1T'$-MoTe$_2$ via DFT does not show any close bands

Figure 4.5: Bandstructures of T_d- and $1T'$-MoTe$_2$ via DFT

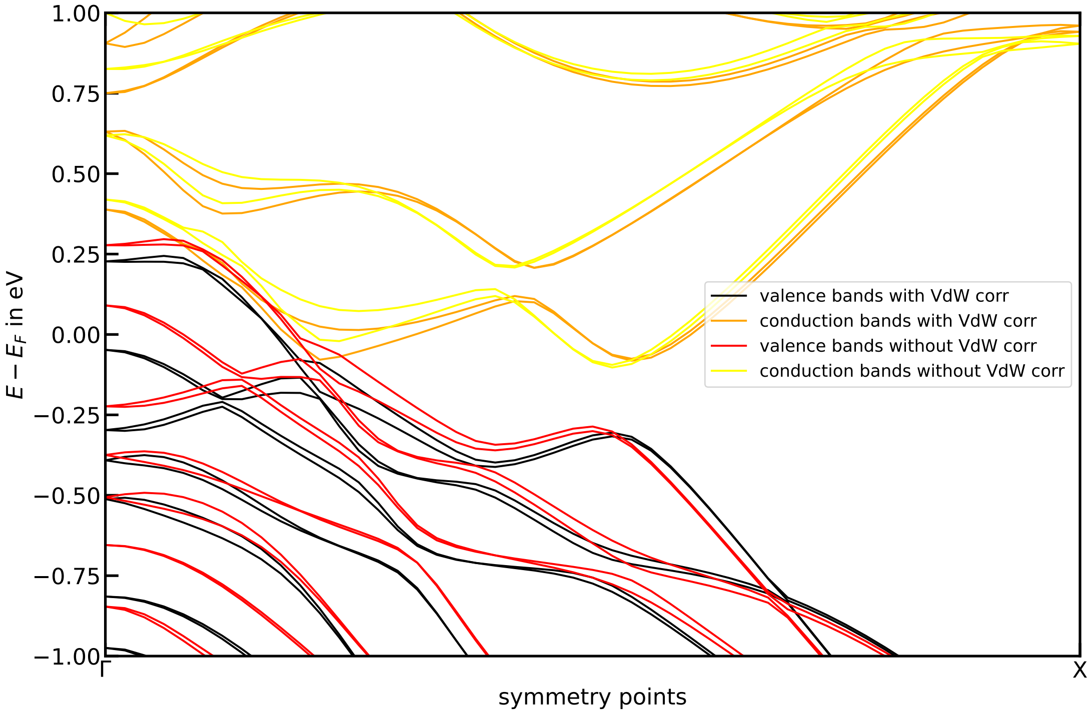

Figure 4.6: Comparison of bandstructure of T_d-MoTe$_2$ with vs. without VdW-correction show significant differences

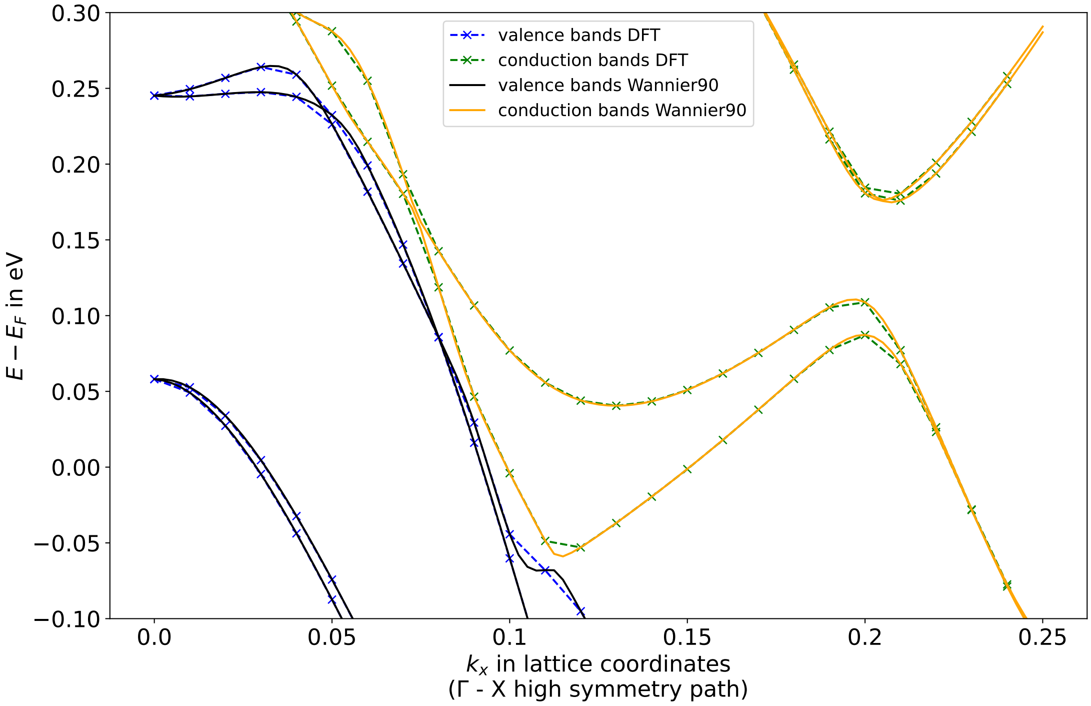

Figure 4.7: Comparison of zoomed in bandstructure of T_d-MoTe$_2$ calculated with DFT vs. W90 show significantly more precision in interpolation

WPs per sector were found. For this purpose, the difference between the adjacent valence and conduction bands was considered.

In fig. 4.8, the difference of the adjacent valence and conduction band in the k_x-k_y plane is shown. Here, in the first quadrant with $k_x \in [0, 0.25]b_1$, $k_y \in [0, 0.25]b_2$, two representative WPs are visible. The energy differences in this section range from approximately 0 to 600 meV. In the black region at the minima, the WPs are located at positions $W_1 = (0.055, 0.0175, 0)$ and $W_2 = (0.095, 0.0525, 0)$ with energy differences of $\Delta E_{W_1} = 1.8$ meV and $\Delta E_{W_2} = 0.6$ meV.

In fig. 4.9, a path through the WPs in the band structure is shown. It can be seen that the WPs are located at $E_{W_1} = 226.9\,\text{meV}$ and $E_{W_2} = 45.8\,\text{meV}$ just above the Fermi energy. In the plot fig. 4.10, depicting the region of the k_x-k_y plane around the WPs, the Weyl-cones are visible, characterizing the material as a type-II-WSM.

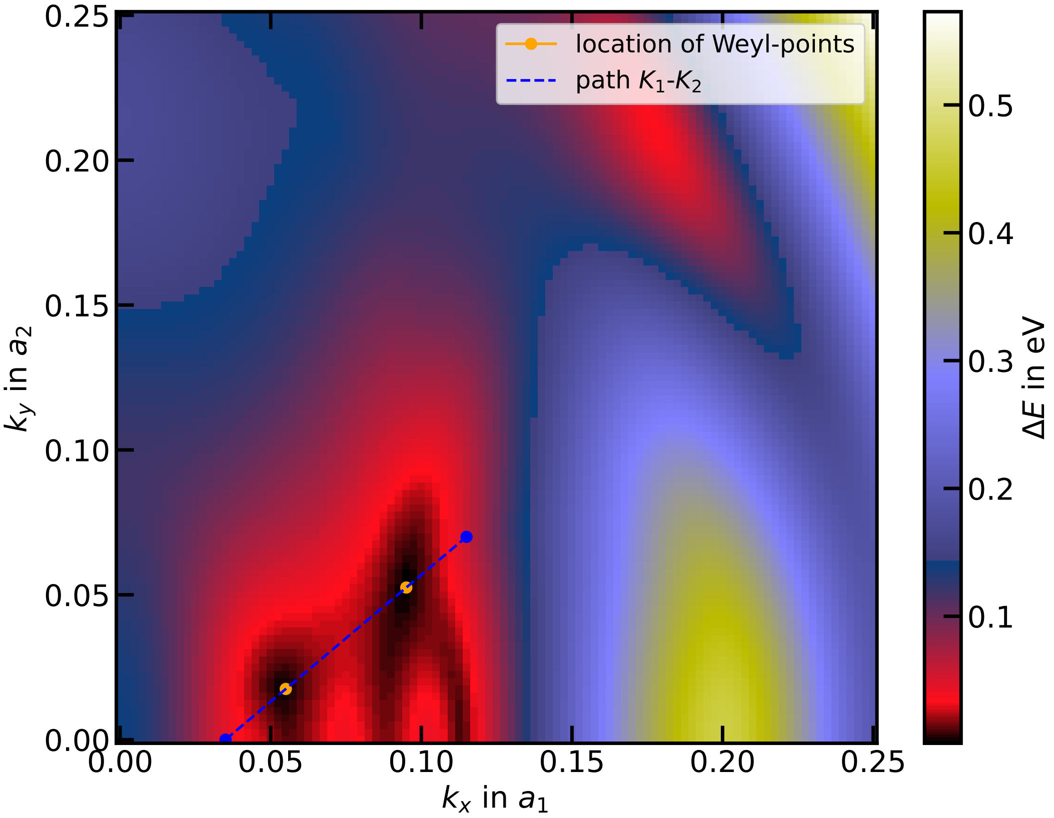

Figure 4.8: Contour plot of energy difference (ΔE) of closest valence and conduction bands in T_d-MoTe$_2$; location of WPs in orange; path $K_1 - K_2$ through WPs in blue depicted in bandstructure in 4.9

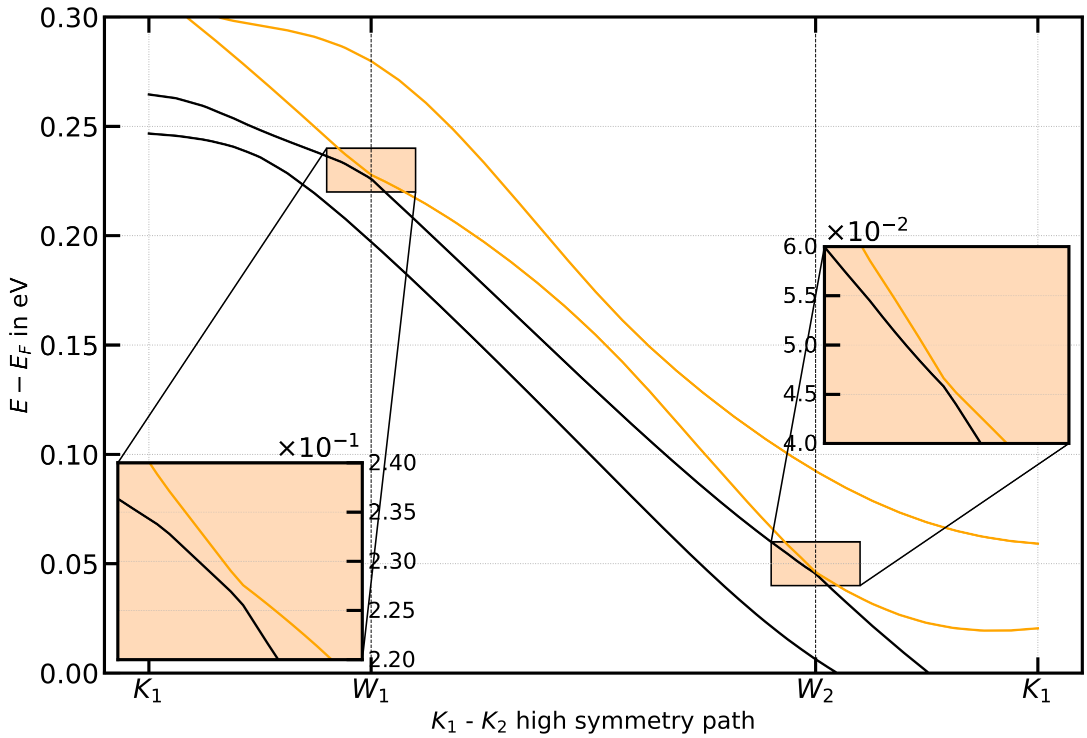

Figure 4.9: Bandstructure of T_d-MoTe$_2$ over path $K_1 - K_2$ show close WPs

4.3 Phonons

The discovery of the WPs in the simulated T_d-MoTe$_2$ inspired the consideration of whether a PT from the T_d phase to the $1T'$ phase via coherent phonons is possible. In the following, it is demonstrated that this transition can indeed be simulated.

4.3.1 Dispersion

In fig. 4.11 the phonon dispersion of T_d-MoTe$_2$ along the above-defined path is shown. The dispersion is plotted against frequency in cm^{-1}. Only the three translational directions are considered, so for twelve atoms 36 vibrational modes are possible. Three of these emerge as acoustic modes, recognizable by the vanishing frequency at the Γ-point. The optical modes can be subdivided into four symmetries or irreducible representations with different characteristics. Good convergence is achieved in this calculation, evident by the absence of negative frequencies (aside from one point on the Y-Γ path).

To enable a PT, displacements in the yz-plane are required. Group-theoretical analysis [31] shows that only the A_1 and B_1 modes are suitable. A few of these lie

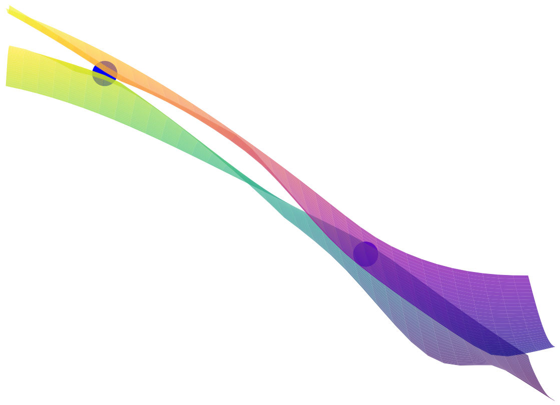

(a) Both WPs in k_x-k_y-plane

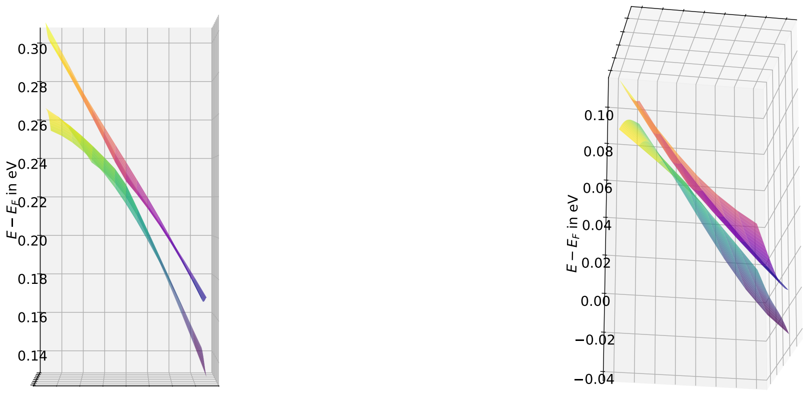

(b) Weyl-cone of WP W_1

(c) Weyl-cone of WP W_2

Figure 4.10: Weyl-cones in k_x-k_y-plane with $E - E_F$ on z-axis

in the low-frequency range below 50 cm^{-1}, while most occur between 80 cm^{-1} and 170 cm^{-1}. In the higher-frequency range of 210 cm^{-1} to 270 cm^{-1} there are four degenerate A_1 and four degenerate B_1 modes. Besides the relevant eleven A_1 and B_1 optical modes, there are also five A_2 and six B_2 modes.

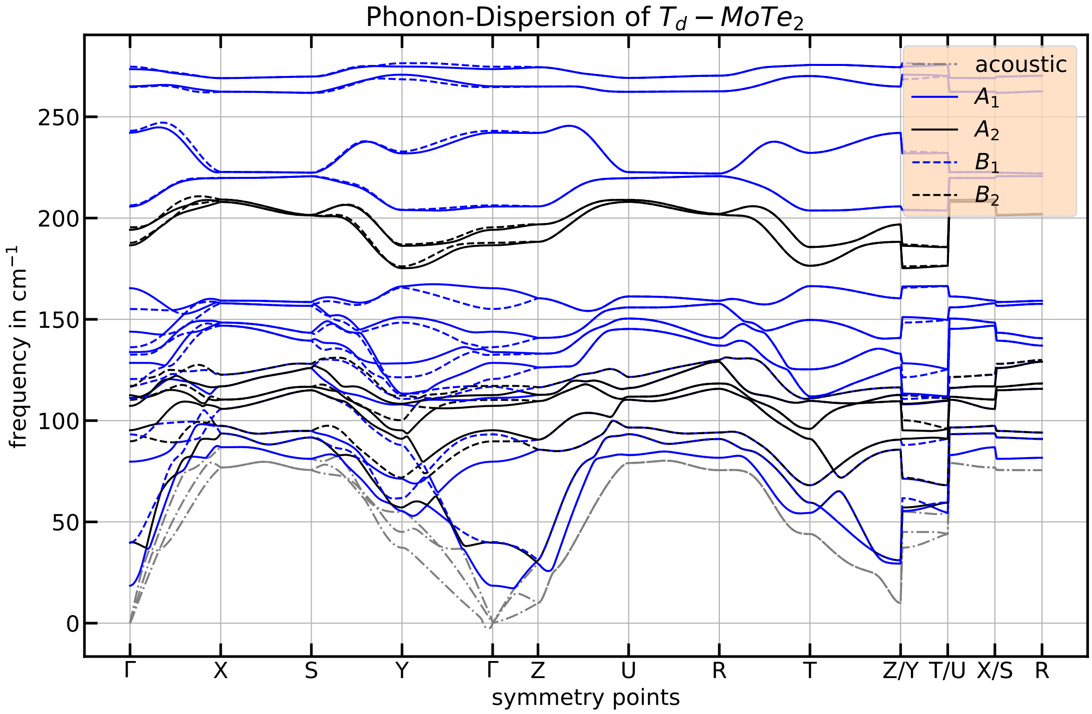

Figure 4.11: Phonondispersion of T_d-MoTe$_2$

4.3.2 Description of coherent modes

The computed modes provide atomic displacements calculated via 2.46 based on the frequencies and eigenvectors. The displacements due to A_1 and B_1 modes are shown in fig. 4.12 and fig. 4.13. All displacements are here in the yz-plane. Most modes appear chaotic, as they shift atoms by varying distances and in different directions. However, there are a few modes that can be described simply. I have numbered the modes in ascending frequency and will use this numbering in the following: **Mode #4** shears the monolayers in the y-direction. This mode could therefore be of particular interest in the investigation. **Mode #6** exhibits a compression of two monolayers towards each other, while another pair moves apart. This motion is rather secondary for the PT. **Modes #9 and #15** partially show an intralayer shear. This movement is also very interesting for the PT.

Table 4.2: Coefficients of contribution for linear combination of phonon mode displacements of T_d-MoTe$_2$; significant contributions by B_1-modes

B_1 #	coefficients	A_1 #	coefficients
6	1.176	4	0.1862
9	-13.839	7	0.0023
15	8.183	13	0.0097
17	-3.237	18	-0.0089
19	-12.127	20	0.0661
21	-1.102	22	-0.9446
23	-2.196	24	0.2703
30	-0.0611	29	-0.0830
32	0.7516	31	-0.2054
33	3.696	34	0.2573
36	1.539	35	0.7026

Overall, there are three modes that appear interesting at first glance.

4.3.3 Linear combinations approximating the phase transition

Mode #4 yielded no PT for any multiple despite its promising appearance.
Modes #9 and #15, combined with **#19** via linear combination, led to the space group $P2_1$ with a numerical accuracy of 10^{-4} in crystal coordinates using spglib. The linear combination was formed as follows:

$$\Delta\tau_{\text{tot}} = -13.72\,\Delta\tau_9 + 8.1\,\Delta\tau_{15} - 12.27\,\Delta\tau_{19}. \tag{4.1}$$

The resulting displacement is shown in fig. 4.14.

For a linear combination of all A_1 and B_1 modes, the coefficients assemble as shown in table 4.2. It is immediately apparent that the influence of the A_1 modes contributes only a few percent to the PT, including mode #4. In contrast, one can see that the relatively large contributions of modes #9, #15, and #19, as shown earlier, enable the PT.

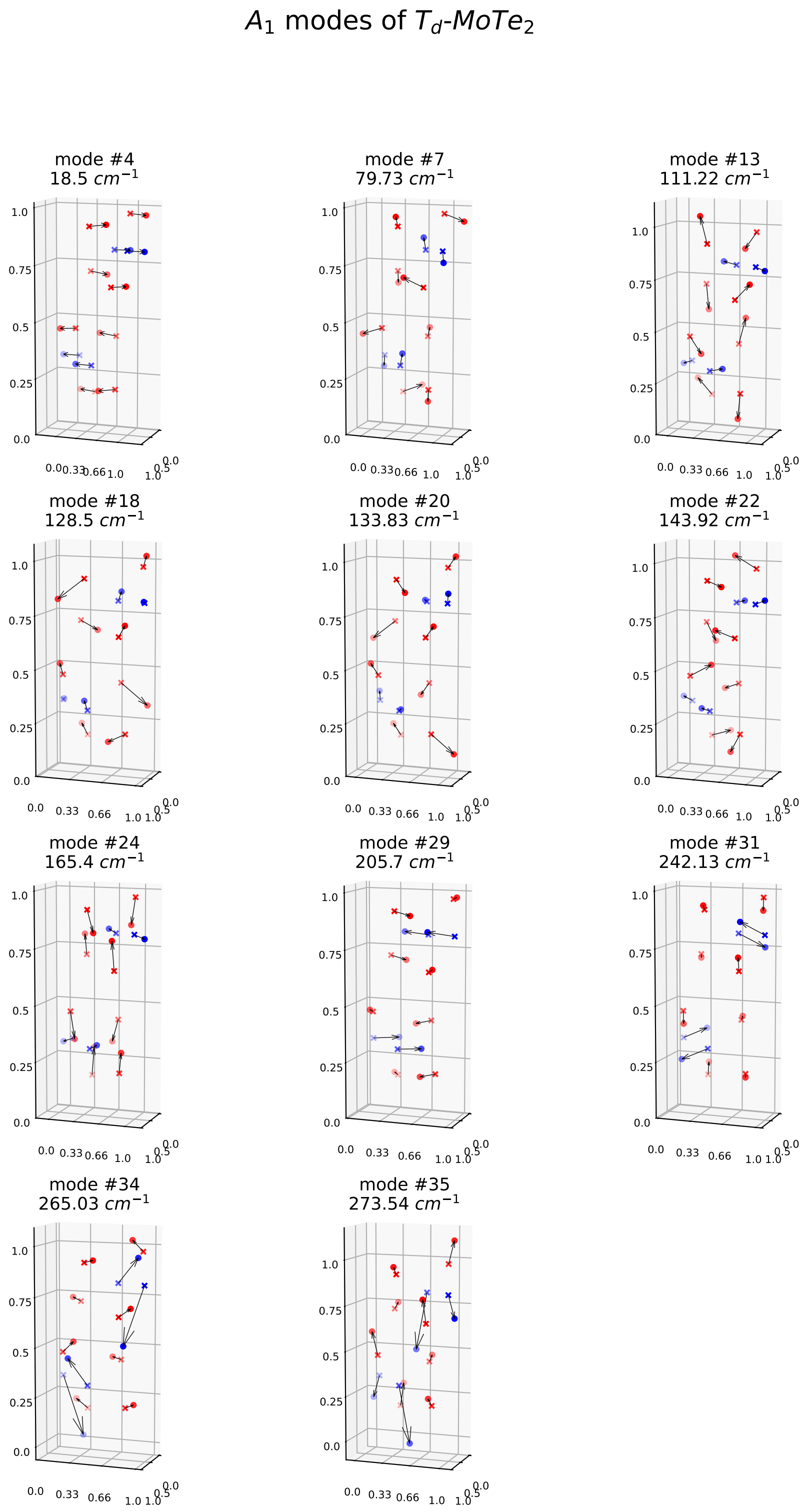

Figure 4.12: Displacement of T_d-MoTe$_2$-atoms by A_1-modes in real space

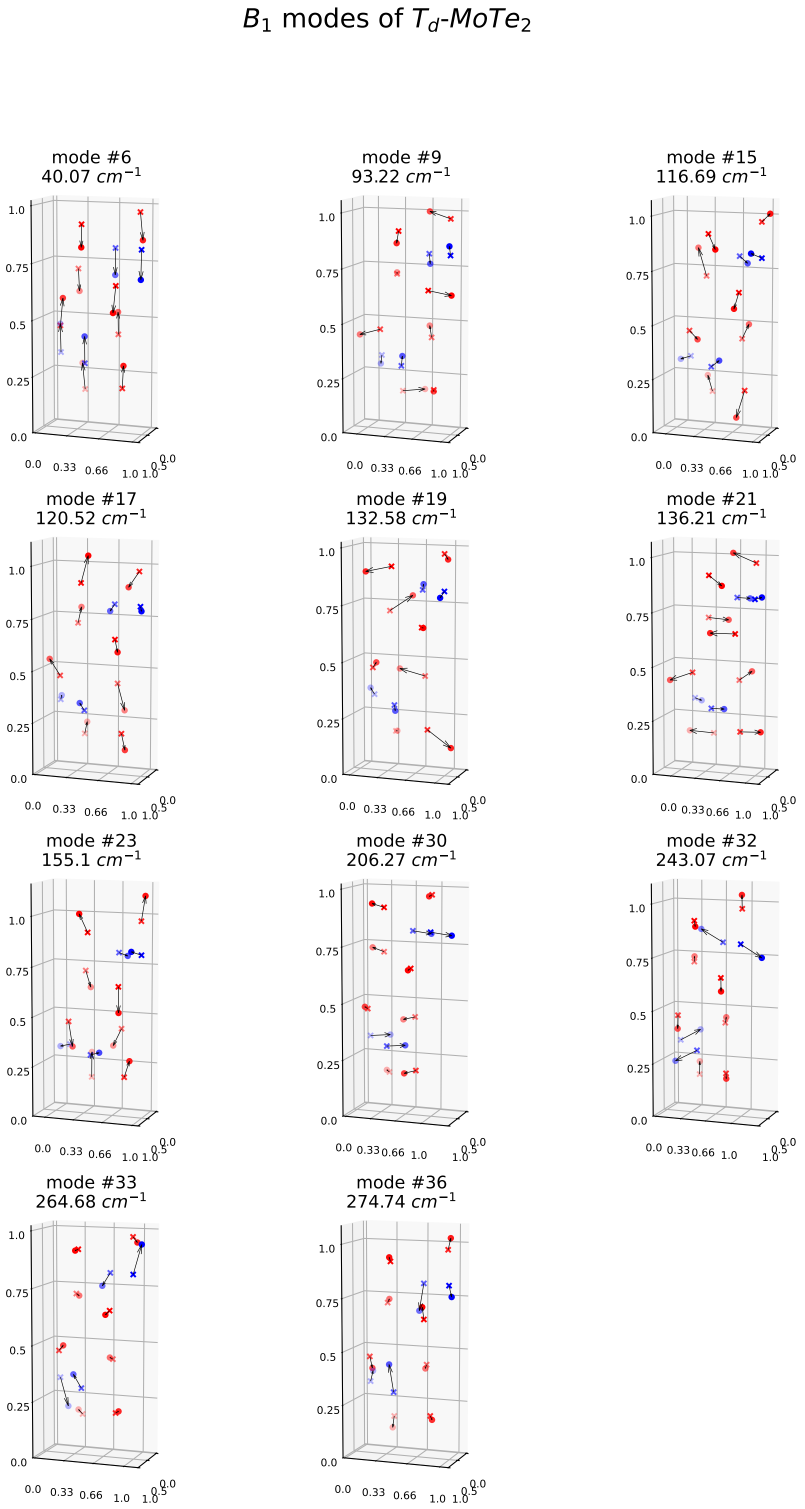

Figure 4.13: Displacement of T_d-MoTe$_2$-atoms by B_1-modes in real space

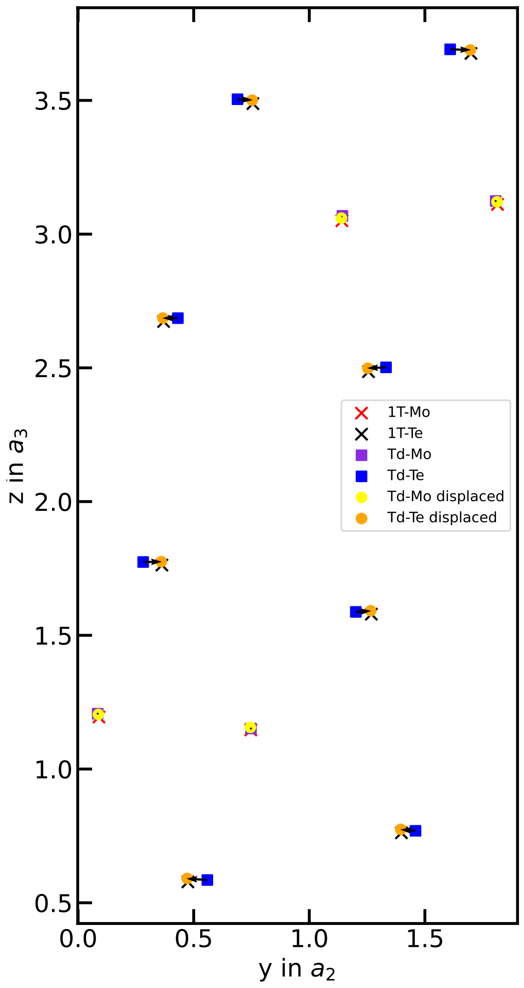

Figure 4.14: Displacement of T_d-MoTe$_2$ to 1T'-phase by linear combination of modes #9, #15 and #19

5 Discussion

After presenting the results of the calculations here, the discussion now turns to comparing experimental and simulated data, interpreting them, and identifying the limitations of the methods.

5.1 Comparison with experimental and simulated data

Since the discovery of the WPs, numerous studies have investigated the WPs in T_d-MoTe$_2$ and other properties of the material. Therefore, there is strong evidence supporting the validity of the calculated band structures.

5.1.1 Comparison of methods

Methodological information in papers is often kept brief, and if there is no supplementary material, sometimes contacting the authors is necessary. Therefore, only freely accessible methods were reviewed and compared.

[44, 45] provide in their papers a rough account of the parameters used for their simulations of the band structures of T_d-MoTe$_2$. [42], on the other hand, offers detailed methodological information in its supplementary material.

All studies employ VASP (*Vienna Ab initio Simulation Package*), a competitor to QE. PAW pseudopotentials including SOC were used, and PBE functionals [37] were employed. Both groups interpolate with MLWFs, so the methods largely agree. [44] additionally use a hybrid functional (HSE06), which is not easily available in QE. Here, E_{cut} was set to 600 eV/450 eV/300 eV ($\approx$ 55 Ry/33 Ry/22 Ry), which is lower than $E_{cut} = 80$ Ry in this work. Their k-point sampling density $n_k = 16 \times 10 \times 4$ is also coarser than the density used here for the band structure. Thus, the results of this work should promise higher accuracy.

The cell volumes of the unit cells in table 5.1 for the T_d phase reported in other

Table 5.1: Comparison of cell parameters of this work with [42] and [44]

	this work	[42]	[44]
a_1 in a_0	6.5184	6.5196	6.5706
a_2 in a_0	11.9205	11.9601	11.9714
a_3 in a_0	24.9900	25.4830	26.2351
Ω in a_0^3	1941.7877	1987.0387	2063.6341

works are larger than the unit cell volume in this work.

5.1.2 Comparison of bandstructures

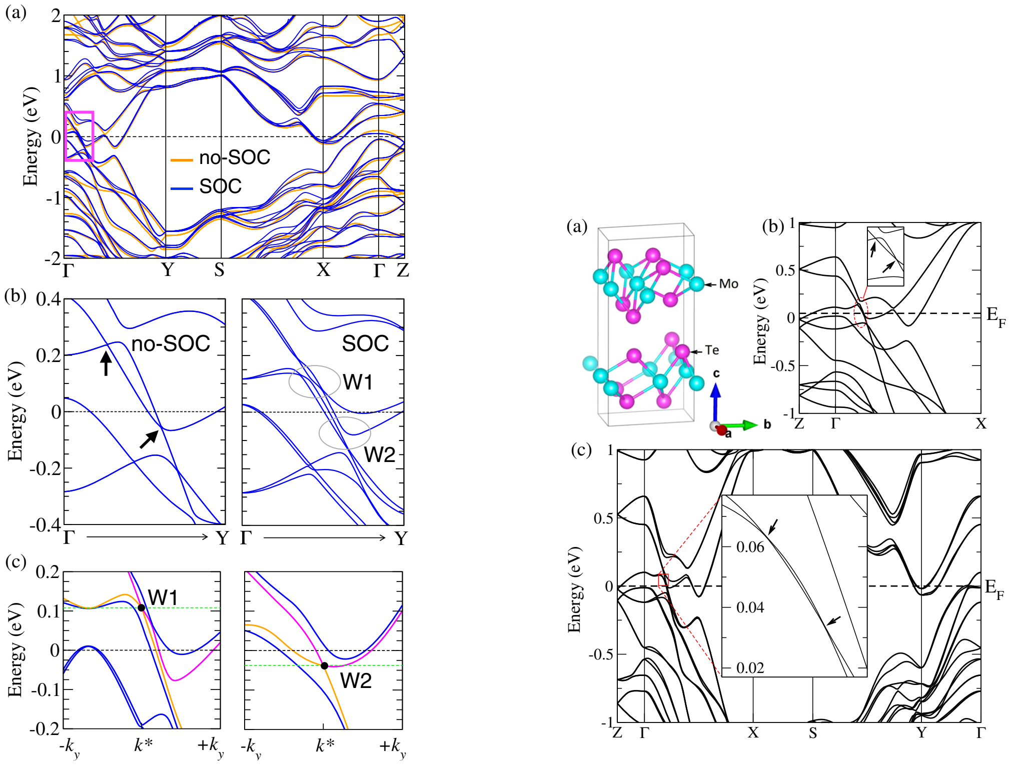

(a) [42]　　(b) [51]

Figure 5.1: [42, 51]

In fig. 5.2 and fig. 5.1, the simulated band structures of T_d-MoTe$_2$ from [44, 42, 51] are shown. The band structure along the path Γ-Y-S-X-Γ-Z exhibits very strong agreement with the results in fig. 4.5a in the corresponding segments. However, when examining the WPs in table 5.2 more closely, one finds a relatively large deviation in their positions and also in their number in k-space. The energy levels and

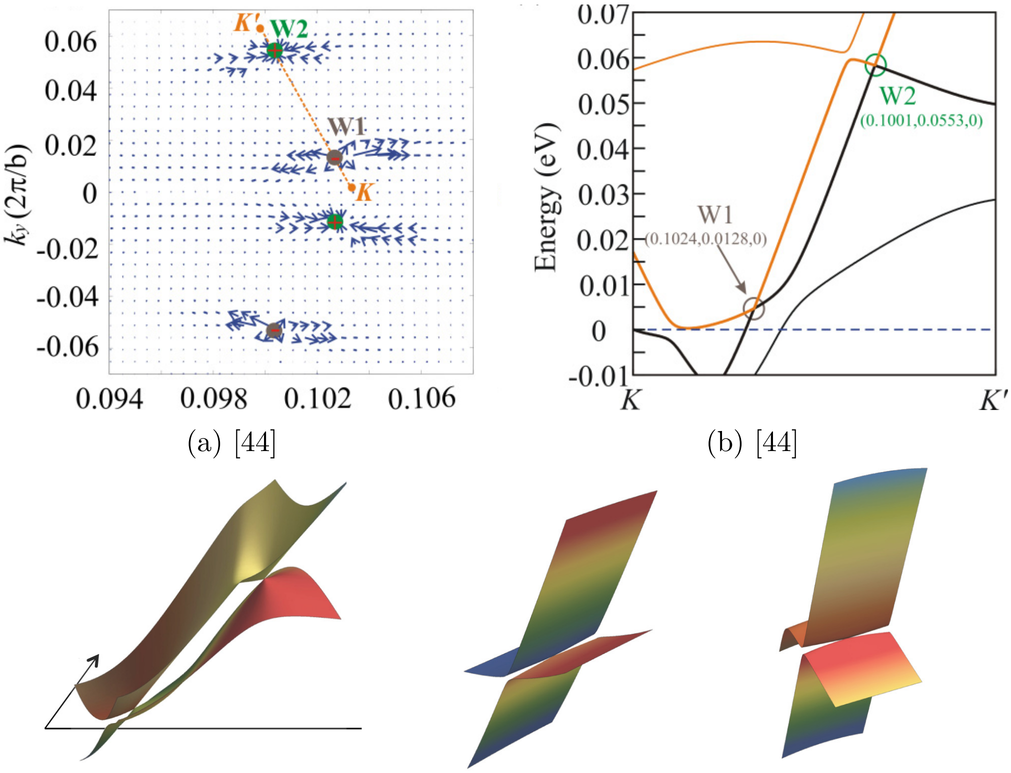

(a) [44]

(b) [44]

(c) [44]

Figure 5.2: [44]

Table 5.2: Comparison of WP positions in momentum space and energy difference in this work vs. [42, 44, 51]

	this work	[42]	[44]	[51]
k_{x_1} in b_1	0.055	-	0.1024	-
k_{y_1} in b_2	0.0175	-	0.0128	-
E_{W_1} in meV	45.8	-	6	-
k_{x_2} in b_1	0.095	0.02	0.1001	0.1011
k_{y_2} in b_2	0.0525	0.068	0.0530	0.0503
E_{W_2} in meV	226.9	108	55	55

differences between the respective WPs also show significant discrepancies, as can be taken from fig. 4.5a.

In fig. 5.2c, the Weyl cones are visible. Here, it is shown that the ratio of the separation in k-space to the energy difference is consistent with the results of this work in fig. 4.10.

5.2 Interpretation of results in the context of current research

In [31], an extensive study on the phonon modes of T_d-MoTe$_2$, $1T'$-MoTe$_2$, and T_d-WTe$_2$ was carried out both experimentally and via simulations. They researched parameters very similar to those in this work. However, a notable difference arises: they reported [11 A_1 + 6 A_2 + 5 B_1 + 11 B_2] modes, such that the indices of the B modes in [31] are swapped relative to this work. This discrepancy may stem from differing definitions of the lattice vectors. A comparison of the B_2-mode frequencies in [31] with the B_1 modes in this work shows only marginal differences. Hence, a reevaluation of the mode characterization may be necessary, but this falls beyond the scope of the present study.

Nevertheless, a comparability of the A_1 modes via the average deviation $\bar{\nu}$ is given. The mode frequencies exhibit only an average deviation of $\bar{\nu} = 7.5$ cm^{-1} or $\frac{\bar{\nu}}{\nu} = 11.4\%$. By closer look at the plot of the experimentally determined phonon modes, the movement of equi-frequency modes can again be recognized compared to fig. 4.12. The mean frequency deviation of the B_1 modes in fig. 4.13 from the B_2 modes [31] is only $\bar{\nu} = 7.1$ cm^{-1} or $\frac{\bar{\nu}}{\nu} = 6.4\%$. Thus, the phonon calculation in this work is at least confirmed by that paper.

Also, [54] determined the same distribution of modes through first-principles calculations and Raman experiments. A comparison yielded $\bar{\nu}_{A_1} = 2.7$ cm^{-1} or $\frac{\bar{\nu}_{A_1}}{\nu_{A_1}} = 4.3\%$, and $\bar{\nu}_{B_1} = 3.0$ cm^{-1} or $\frac{\bar{\nu}_{B_1}}{\nu_{B_1}} = 2.4\%$.

They found five modes in T_d-MoTe$_2$ with similar frequencies in 1T′-MoTe$_2$, whose displacements show remarkable similarities. Their conclusion was that a temperature-induced PT would be readily achievable.

Neither paper investigated a light-induced PT. In particular, the insight from [54] provides impetus for further studies.

[14] report a shear mode in $1T'$-MoTe$_2$ that has until now only been observed in T_d-MoTe$_2$. The frequency and shear character are comparable to the A_1 shear mode found here ($\nu_{A_1^1} = 18.5$ cm^{-1}). They speculated that a light-induced PT via this mode might be possible. However, the results of the present work do not support this hypothesis.

[41] achieved a light-induced PT in WTe$_2$ via a low-frequency A_1 shear mode. Since this TMD exhibits very similar properties to MoTe$_2$, further investigation of the equivalent A_1^1 mode in MoTe$_2$ is essential.

In contrast, 4.14 clearly shows that a theoretical PT could be enabled by B_1 modes (characterized as B_2 in other works). Whether these modes are experimentally capable of inducing a PT remains unclear.

5.3 Limitations of the methods

The confirmation of WPs (with opposite chirality) by sources and sinks in the Berry curvature would have supported the results. However, neither QE nor W90 offer a way to perform a band-resolved analysis of the Berry curvature. For that, another tool such as *Wannier_Tools* would need to be employed.

Similarly, a comparison with experimentally determined WPs via a k-space resolved density of states would have provided another solid validation of my results. Again, these programs do not offer this capability.

Using TR-ARPES, [19] have already observed an approach to a light-induced PT via an A_1 shear mode in WTe$_2$. However, a full transition could not be detected. The method of time-resolved simulations also occurred to me.

These aspects were primarily constrained by the time limitations inherent to a bachelor's thesis.

6 Conclusion and Outlook

In this work, the electronic structure and lattice vibrational dynamics of $\mathrm{MoTe_2}$ in the T_d phase were systematically investigated using *ab-initio* methods. Through DFT calculations combined with SOC and Wannier interpolation, the existence of two Weyl points per quadrant of the Brillouin zone was identified. These points lie energetically just above the Fermi level and confirm the topological nature of the T_d phase.

By applying DFPT, the full phonon dispersion of the system was determined. A particular focus was placed on the coherent low-frequency B_1 shear modes, which in this work were identified as the decisive driving force for the structural PT to the centrosymmetric $1T'$ phase. The analysis of linear combinations of these modes demonstrated that targeted atomic displacements enable the transition to the space group $P2_1$. This constitutes a theoretical demonstration that an ultrafast, phonon-induced topological switch in $\mathrm{MoTe_2}$ is achievable.

Despite the results achieved, there are several limitations. In particular, electronic correlations beyond the standard GGA functional were not considered, and the influence of temperature-related entropy contributions on the phase stability remained unaddressed. Furthermore, no explicit coupling between electronic and phononic dynamics on ultrafast laser-pulse timescales, as relevant in real experiments, was performed.

A possible outlook is therefore to extend this study via *ab-initio* molecular dynamics or time-dependent DFT (TDDFT) to model nonlinear effects and realistic excitation conditions. Furthermore, an extension to topological invariants such as the calculation of Chern numbers or Berry curvature would be an interesting way to quantify the topological properties of the individual phases more precisely.

In the long term, the results presented here provide a theoretical foundation for the development of topological switching devices based on $\mathrm{MoTe_2}$ and similar TMDs. The controlled induction of PTs via coherent phonons opens new perspectives in spintronics and quantum information processing, particularly with regard to ultra-compact, energy-efficient, and fault-tolerant devices.

7 Danksagung

Ich möchte mich herzlich bei Prof. Dr. Caruso für die wertvolle Betreuung und Unterstützung während meiner Bachelorarbeit bedanken. Ein großes Dankeschön geht auch an meine Arbeitsgruppe, insbesondere Christoph Emeis und Yiming Pan, für ihre hilfreichen Gespräche, den fachlichen Austausch und die angenehme Zusammenarbeit. Ebenso danke ich meinen Freunden und meiner Familie für ihre Motivation, ihr Verständnis und ihre stetige Unterstützung. Ihr habt mir geholfen, auch in stressigen Zeiten den Fokus zu behalten.

8 Erklärung über eigenständige Arbeit

Hiermit erkläre ich, dass ich die vorliegende Arbeit selbstständig und nur unter Verwendung der angegebenen Quellen und Hilfsmittel angefertigt habe. Alle wörtlich oder sinngemäß übernommenen Stellen sind als solche kenntlich gemacht. Die Arbeit wurde in gleicher oder ähnlicher Form noch keiner anderen Prüfungsbehörde vorgelegt und nicht veröffentlicht.

Datum, Unterschrift: ______________________________

List of Figures

List of Tables

Bibliography

[1] M. I. Aroyo et al. “Bilbao Crystallographic Server. II. Representations of Crystallographic Point Groups and Space Groups”. In: *Acta Crystallographica Section A: Foundations of Crystallography* (Mar. 2006). DOI: `10.1107/S0108767305040286`.

[2] Mois Ilia Aroyo et al. “Bilbao Crystallographic Server: I. Databases and Crystallographic Computing Programs”. In: *Zeitschrift für Kristallographie - Crystalline Materials* (Jan. 2006). DOI: `10.1524/zkri.2006.221.1.15`.

[3] Edwin Barnes, J. J. Heremans, and Djordje Minic. “Electromagnetic Signatures of the Chiral Anomaly in Weyl Semimetals”. In: *Physical Review Letters* (Nov. 2016). DOI: `10.1103/PhysRevLett.117.217204`.

[4] Michael Berry. *Quantal Phase Factors Accompanying Adiabatic Changes.* 1984. DOI: `10.1098/rspa.1984.0023`.

[5] Felix Bloch. “Über die Quantenmechanik der Elektronen in Kristallgittern”. In: *Zeitschrift für Physik* (July 1929). DOI: `10.1007/BF01339455`.

[6] M. Born and R. Oppenheimer. “Zur Quantentheorie Der Molekeln”. In: *Annalen der Physik* (1927). DOI: `10.1002/andp.19273892002`.

[7] B. E. Brown. “The Crystal Structures of WTe_2 and High-Temperature $MoTe_2$”. In: *Acta Crystallographica* (Feb. 1966). DOI: `10.1107/S0365110X66000513`.

[8] A. A. Burkov. “Anomalous Hall Effect in Weyl Metals”. In: *Physical Review Letters* (Oct. 2014). DOI: `10.1103/PhysRevLett.113.187202`.

[9] Fabio Caruso. *Phonon Lecture.* 2025.

[10] Fabio Caruso and Marios Zacharias. “Quantum Theory of Light-Driven Coherent Lattice Dynamics”. In: *Physical Review B* (Feb. 2023). DOI: `10.1103/PhysRevB.107.054102`.

[11] Ching-Kit Chan et al. “When Chiral Photons Meet Chiral Fermions: Photoinduced Anomalous Hall Effects in Weyl Semimetals”. In: *Physical Review Letters* (Jan. 2016). DOI: `10.1103/PhysRevLett.116.026805`.

[12] Ke Deng et al. “Experimental Observation of Topological Fermi Arcs in Type-II Weyl Semimetal $MoTe_2$”. In: *Nature Physics* (Dec. 2016). DOI: `10.1038/nphys3871`.

[13] Ya Deng et al. “$MoTe_2$: Semiconductor or Semimetal?” In: *ACS Nano* (Aug. 2021). DOI: `10.1021/acsnano.1c01816`.

[14] Takumi Fukuda et al. “Ultrafast Dynamics of the Low Frequency Shear Phonon in 1T′-$MoTe_2$”. In: *Applied Physics Letters* (Mar. 2020). DOI: `10.1063/1.5143485`.

[15] P Giannozzi et al. “Advanced Capabilities for Materials Modelling with Quantum ESPRESSO”. In: *Journal of Physics: Condensed Matter* (Oct. 2017). DOI: `10.1088/1361-648X/aa8f79`.

[16] Paolo Giannozzi et al. “QUANTUM ESPRESSO: A Modular and Open-Source Software Project for Quantum Simulations of Materials”. In: *Journal of Physics: Condensed Matter* (Sept. 2009). DOI: `10.1088/0953-8984/21/39/395502`.

[17] Feliciano Giustino. *Materials Modelling Using Density Functional Theory: Properties and Predictions.* Oxford University Press. 2014.

[18] Stefan Grimme et al. “A Consistent and Accurate Ab Initio Parametrization of Density Functional Dispersion Correction (DFT-D) for the 94 Elements H-Pu”. In: *The Journal of Chemical Physics* (Apr. 2010). DOI: `10.1063/1.3382344`.

[19] Petra Hein et al. “Mode-Resolved Reciprocal Space Mapping of Electron-Phonon Interaction in the Weyl Semimetal Candidate Td-WTe2”. In: *Nature Communications* (May 2020). DOI: `10.1038/s41467-020-16076-0`.

[20] Conyers Herring. “Accidental Degeneracy in the Energy Bands of Crystals”. In: *Physical Review* (Aug. 1937). DOI: `10.1103/PhysRev.52.365`.

[21] Yoyo Hinuma et al. “Band Structure Diagram Paths Based on Crystallography”. In: *Computational Materials Science* (Feb. 2017). DOI: `10.1016/j.commatsci.2016.10.015`.

[22] P. Hohenberg and W. Kohn. “Inhomogeneous Electron Gas”. In: *Physical Review* (Nov. 1964). DOI: `10.1103/PhysRev.136.B864`.

[23] Lunan Huang et al. “Spectroscopic Evidence for a Type II Weyl Semimetallic State in $MoTe_2$”. In: *Nature Materials* (Nov. 2016). DOI: `10.1038/nmat4685`.

[24] Shin-Ming Huang et al. “A Weyl Fermion Semimetal with Surface Fermi Arcs in the Transition Metal Monopnictide TaAs Class”. In: *Nature Communications* (June 2015). DOI: `10.1038/ncomms8373`.

[25] Shin-Ming Huang et al. “An Inversion Breaking Weyl Semimetal State in the TaAs Material Class”. In: *Nat. Commun.* (Jan. 2015).

[26] Xiaochun Huang et al. “Observation of the Chiral-Anomaly-Induced Negative Magnetoresistance in 3D Weyl Semimetal TaAs”. In: *Physical Review X* (Aug. 2015). DOI: `10.1103/PhysRevX.5.031023`.

[27] Anubhav Jain et al. “Commentary: The Materials Project: A Materials Genome Approach to Accelerating Materials Innovation”. In: *APL Materials* (July 2013). DOI: `10.1063/1.4812323`.

[28] W. Kohn and L. J. Sham. “Self-Consistent Equations Including Exchange and Correlation Effects”. In: *Physical Review* (Nov. 1965). DOI: `10.1103/PhysRev.140.A1133`.

[29] Hiroshi Kohno. “Spintronics with Weyl Semimetal”. In: *JPSJ News and Comments* (Jan. 2021). DOI: `10.7566/JPSJNC.18.13`.

[30] Yupeng Li et al. “Negative Magnetoresistance in Weyl Semimetals NbAs and NbP: Intrinsic Chiral Anomaly and Extrinsic Effects”. In: *Frontiers of Physics* (June 2017). DOI: `10.1007/s11467-016-0636-8`.

[31] Xiaoli Ma et al. “Raman Scattering in the Transition-Metal Dichalcogenides of 1T’-MoTe$_2$, T$_2$MoTe$_2$, and T$_2$WTe$_2$”. In: *Physical Review B* (Dec. 2016). DOI: `10.1103/PhysRevB.94.214105`.

[32] Yonatan Messica, Dmitri B. Gutman, and Pavel M. Ostrovsky. “Anomalous Hall Effect in Disordered Weyl Semimetals”. In: *Physical Review B* (July 2023). DOI: `10.1103/PhysRevB.108.045121`.

[33] Koichi Momma and Fujio Izumi. “VESTA: A Three-Dimensional Visualization System for Electronic and Structural Analysis”. In: *Journal of Applied Crystallography - J APPL CRYST* (June 2008). DOI: `10.1107/S0021889808012016`.

[34] S. Nandy et al. “Chiral Anomaly as the Origin of the Planar Hall Effect in Weyl Semimetals”. In: *Physical Review Letters* (Oct. 2017). DOI: `10.1103/PhysRevLett.119.176804`.

[35] H.B. Nielsen and Masao Ninomiya. “The Adler-Bell-Jackiw Anomaly and Weyl Fermions in a Crystal”. In: *Physics Letters B* (Nov. 1983). DOI: `10.1016/0370-2693(83)91529-0`.

[36] E Pehlke. “Grundkonzepte der Theoretischen Festkörperphysik”. In: (June 2025).

[37] John P. Perdew, Kieron Burke, and Matthias Ernzerhof. “Generalized Gradient Approximation Made Simple”. In: *Physical Review Letters* (Oct. 1996). DOI: `10.1103/PhysRevLett.77.3865`.

[38] Giovanni Pizzi et al. “Wannier90 as a Community Code: New Features and Applications”. In: *Journal of Physics: Condensed Matter* (Jan. 2020). DOI: `10.1088/1361-648X/ab51ff`.

[39] Yanpeng Qi et al. “Superconductivity in Weyl Semimetal Candidate MoTe2”. In: *Nature Communications* (Mar. 2016). DOI: `10.1038/ncomms11038`. arXiv: `1508.03502 [cond-mat]`.

[40] Xiaofeng Qian et al. “Quantum Spin Hall Effect and Topological Field Effect Transistor in Two-Dimensional Transition Metal Dichalcogenides”. In: *Science* (Dec. 2014). DOI: `10.1126/science.1256815`. arXiv: `1406.2749 [cond-mat]`.

[41] Edbert J. Sie et al. “An Ultrafast Symmetry Switch in a Weyl Semimetal”. In: *Nature* (Jan. 2019). DOI: `10.1038/s41586-018-0809-4`.

[42] Sobhit Singh et al. “Engineering Weyl Phases and Nonlinear Hall Effects in T d - MoTe$_2$”. In: *Physical Review Letters* (July 2020). DOI: `10.1103/PhysRevLett.125.046402`.

[43] Alexey A. Soluyanov et al. “Type-II Weyl Semimetals”. In: *Nature* (Nov. 2015). DOI: `10.1038/nature15768`.

[44] Yan Sun et al. “Prediction of Weyl Semimetal in Orthorhombic MoTe$_2$”. In: *Physical Review B* (Oct. 2015). DOI: `10.1103/PhysRevB.92.161107`.

[45] A. Tamai. “Fermi Arcs and Their Topological Character in the Candidate Type-II Weyl Semimetal MoTe$_2$”. In: *Physical Review X* (2016). DOI: `10.1103/PhysRevX.6.031021`.

[46] Xinsheng Tan et al. “Simulation and Manipulation of Tunable Weyl-Semimetal Bands Using Superconducting Quantum Circuits”. In: *Physical Review Letters* (Jan. 2019). DOI: `10.1103/PhysRevLett.122.010501`.

[47] E. S. Tasci et al. “An Introduction to the Tools Hosted in the Bilbao Crystallographic Server”. In: *EPJ Web of Conferences* (2012). DOI: `10.1051/epjconf/20122200009`.

[48] D. J. Thouless et al. “Quantized Hall Conductance in a Two-Dimensional Periodic Potential”. In: *Physical Review Letters* (Aug. 1982). DOI: `10.1103/PhysRevLett.49.405`.

[49] Atsushi Togo, Kohei Shinohara, and Isao Tanaka. *$\texttt{Spglib}$: A Software Library for Crystal Symmetry Search.* Mar. 2024. DOI: `10.48550/arXiv.1808.01590`. arXiv: `1808.01590 [cond-mat]`.

[50] Xiangang Wan et al. "Topological Semimetal and Fermi-arc Surface States in the Electronic Structure of Pyrochlore Iridates". In: *Physical Review B* (May 2011). DOI: `10.1103/PhysRevB.83.205101`.

[51] Zhijun Wang et al. "$MoTe_2$: A Type-II Weyl Topological Metal". In: *Physical Review Letters* (July 2016). DOI: `10.1103/PhysRevLett.117.056805`.

[52] Hermann Weyl. "Elektron und Gravitation. I". In: *Zeitschrift für Physik* (May 1929). DOI: `10.1007/BF01339504`.

[53] Thorsten Zandt et al. "Quadratic Temperature Dependence up to 50 K of the Resistivity of Metallic $MoTe_2$". In: *Journal of Alloys and Compounds - J ALLOYS COMPOUNDS* (Sept. 2007). DOI: `10.1016/j.jallcom.2006.09.157`.

[54] Kenan Zhang et al. "Raman Signatures of Inversion Symmetry Breaking and Structural Phase Transition in Type-II Weyl Semimetal $MoTe_2$". In: *Nature Communications* (Dec. 2016). DOI: `10.1038/ncomms13552`. arXiv: `1606.05071 [cond-mat]`.